

AD _____

Award Number: DAMD17-98-1-8147

TITLE: Breast Cancer Screening Using Photonic Technology

PRINCIPAL INVESTIGATOR: Robert R. Alfano, Ph.D.
S. K. Gayen
M. Alrubaiee
W. Cai
J. A. Koutcher

CONTRACTING ORGANIZATION: The Research Foundation of the City
University of New York
New York, New York 10031-9198

REPORT DATE: March 2003

TYPE OF REPORT: Final

PREPARED FOR: U.S. Army Medical Research and Materiel Command
Fort Detrick, Maryland 21702-5012

DISTRIBUTION STATEMENT: Approved for Public Release;
Distribution Unlimited

The views, opinions and/or findings contained in this report are those of the author(s) and should not be construed as an official Department of the Army position, policy or decision unless so designated by other documentation.

20030904 094

REPORT DOCUMENTATION PAGEForm Approved
OMB No. 074-0188

Public reporting burden for this collection of information is estimated to average 1 hour per response, including the time for reviewing instructions, searching existing data sources, gathering and maintaining the data needed, and completing and reviewing this collection of information. Send comments regarding this burden estimate or any other aspect of this collection of information, including suggestions for reducing this burden to Washington Headquarters Services, Directorate for Information Operations and Reports, 1215 Jefferson Davis Highway, Suite 1204, Arlington, VA 22202-4302, and to the Office of Management and Budget, Paperwork Reduction Project (0704-0188), Washington, DC 20503

1. AGENCY USE ONLY (Leave blank)		2. REPORT DATE March 2003	3. REPORT TYPE AND DATES COVERED Final (15 Aug 98 - 14 Feb 03)	
4. TITLE AND SUBTITLE Breast Cancer Screening Using Photonic Technology			5. FUNDING NUMBERS DAMD17-98-1-8147	
6. AUTHOR(S) Robert R. Alfano, Ph.D., S. K. Gayen, M. Alrubaiee, W. Cai, J. A. Koutcher				
7. PERFORMING ORGANIZATION NAME(S) AND ADDRESS(ES) The Research Foundation of the City University of New York New York, New York 10031-9198 E-Mail: alfano@sci.ccnyc.cuny.edu			8. PERFORMING ORGANIZATION REPORT NUMBER	
9. SPONSORING / MONITORING AGENCY NAME(S) AND ADDRESS(ES) U.S. Army Medical Research and Materiel Command Fort Detrick, Maryland 21702-5012			10. SPONSORING / MONITORING AGENCY REPORT NUMBER	
11. SUPPLEMENTARY NOTES				
12a. DISTRIBUTION / AVAILABILITY STATEMENT Approved for Public Release; Distribution Unlimited				12b. DISTRIBUTION CODE
13. Abstract (Maximum 200 Words) (abstract should contain no proprietary or confidential information) <p>The research carried out on this project was aimed at developing noninvasive optical detection and diagnostic methods for breast cancer. The approaches that were developed and pursued include: (a) time-sliced near-infrared (NIR) two dimensional (2-D) transillumination imaging for direct imaging of tumors, and generating data with robust information content for 3-D image reconstruction; (b) spectroscopic 2-D NIR transillumination imaging for exploring the diagnostic potential of optical approach; (c) derivation of analytical solutions of radiative transport equation (RTE) and development of inversion algorithms for reconstruction of 3-D tomographic images using a sequence of time-sliced 2-D images. Results of direct imaging measurements on ex vivo tumor and normal tissues were compared with biopsy, pathology, and nuclear magnetic resonance results for validation. Images recorded with earlier temporal slices of transmitted light were found to highlight cancerous tissues while those recorded with later slices accentuated normal fibrous tissues. Spectroscopic imaging experiments show that the ratio, R of light intensity transmitted through the cancerous tissue to that through the corresponding normal tissue exhibit a wavelength dependent variation that has the potential to be used as a useful parameter for cancer identification. Analytical solutions of RTE enable more complete description of light transport through tissue and forward models based on these solutions promise more accurate and agile 3-D image reconstruction schemes.</p>				
14. SUBJECT TERMS breast cancer, optical mammography, time-resolved imaging, near-infrared imaging, inverse image reconstruction, spectroscopic imaging, NMR, light propagation through turbid media				15. NUMBER OF PAGES 39
				16. PRICE CODE
17. SECURITY CLASSIFICATION OF REPORT Unclassified	18. SECURITY CLASSIFICATION OF THIS PAGE Unclassified	19. SECURITY CLASSIFICATION OF ABSTRACT Unclassified	20. LIMITATION OF ABSTRACT Unlimited	

NSN 7540-01-280-5500

Standard Form 298 (Rev. 2-89)
Prescribed by ANSI Std. Z39-18
298-102

(3)TABLE OF CONTENTS

	<u>Page</u>
1. Front Cover	1
2. SF 298	2
3. Table of Contents	3
4. Introduction	4
5. Body	4
5.1. Setting up and Evaluation of Experimental Arrangements	4
5.2. Time-sliced Direct Imaging of <i>ex vivo</i> Normal and Cancerous Human Breast Tissues	5
5.3. Spectroscopic Direct Imaging of <i>ex vivo</i> Normal and Cancerous Human Breast Tissues	5
5.4. Development of Analytical Solution of Radiative Transport Equation	6
5.5. Development and Demonstration of Inverse Image Reconstruction	6
5.6. Correlation with Existing Methods	7
6. Key Research Accomplishments	7
7. Reportable Outcomes	8
8. Conclusions	11
9. References	12
10. Appendices	
Appendix 1 Reprint: "Photon transport forward model ..."	A1-1
Appendix 2 Reprint: "Parotid gland tissues ... imaging techniques"	A2-1
Appendix 3 Preprint: "Diffusion coefficient ... not on absorption"	A3-1
Appendix 4 Reprint: "Photon migration in ... to radiative transfer"	A4-1
Appendix 5 Preprint: "Cancerous and normal ... imaging techniques"	A5-1

:(4) INTRODUCTION

The goal of the “**Breast Cancer Screening Using Photonic Technology**” research project was to develop optical imaging techniques that make use of noninvasive near-infrared (NIR) light for obtaining direct two-dimensional (2-D), and tomographic three-dimensional (3-D) images of cancerous lesions of human breast. The imaging method involved illuminating the specimen with ultrashort NIR pulses of laser light and construction of images using two approaches. The **time-sliced direct** or the **shadowgram** method utilized the image bearing component of the forward-transmitted light, while the **inverse reconstruction method** made use of the measured transmitted, forward-scattered or backscattered light intensity profiles, known or estimated optical properties of the sample, a model for light propagation through turbid media and a sophisticated computer algorithm to construct images of the interior structure of the specimen.

Significant advances were made not only in developing and testing both of these approaches, but also in demonstrating the diagnostic potential of the **NIR spectroscopic imaging**, as well as, deriving **analytical solutions of radiative transport equation (RTE)** and **development of image reconstruction algorithms** for constructing 3-D images. In order to assess the efficacy of the photonics approach, the photonics experimental results were compared and correlated with that from histopathology and nuclear magnetic resonance (NMR). The results are intriguing and photonics approach highly promising.

This final report covering the research carried out during the entire period of the grant is organized as follows. An overview of the work reported in the three Annual Reports¹⁻³ will be presented for completeness, and the details will be referred to those reports. The work carried out since the last report will be presented in more detail. References to appended publications will be made for detailed descriptions of specific technical aspects of the research. The research accomplishments associated with tasks outlined in the approved Statement of Work (SOW) will be presented in the “**BODY**” Section. “**KEY RESEARCH ACCOMPLISHMENTS**” will present a bulleted list of the major accomplishments resulting from this research. A list of publications, presentations, employment and research opportunities and other deliverables emanating from this research will appear in the “**REPORTABLE OUTCOME**” Section. The importance and implications of the completed research will be summarized in the “**CONCLUSIONS**” Section. Finally, all references pertinent to the report will be presented in the “**REFERENCES**” Section.

(5) BODY

The research carried out, tasks performed, and progress made over the duration of the project may be broadly grouped as follows:

- 5.1. Setting up and Evaluation of Experimental Arrangements;
- 5.2. Time-sliced Direct Imaging of *ex vivo* Normal and Cancerous Human Breast Tissues;
- 5.3. Spectroscopic Direct Imaging of *ex vivo* Normal and Cancerous Human Breast Tissues;
- 5.4. Development of Analytical Solutions of Radiative Transport Equation;
- 5.5. Development and Demonstration of Inverse Image Reconstruction; and
- 5.6. Correlation with Existing Methods.

We will present a brief description of our accomplishments in each of these areas and refer to appended articles and reports for details.

5.1. Setting up and Evaluation of Experimental Arrangements

A major thrust in the initial phase of the project, as detailed in the approved Statement of Work (SOW), was to set up, and evaluate two different types of experimental arrangements for *time-sliced imaging* [**Technical Objectives (TO) 1,2, and 3; Tasks 1-7**]. Both the arrangements used a femtosecond Ti:sapphire laser and amplifier system⁴ for sample illumination, but differed in the signal detection scheme. One of the detection schemes was based on an *ultrafast gated intensified camera system* (UGICS), which provided an electronic time gate with a minimum gate-width of 80 ps and whose position could be varied over a 20-ns interval [**TO3, Tasks 5-7**]. The second approach [**TO1, Tasks 1-3**] used an optical Kerr gate (OKG),⁵ along with a Fourier space gate,⁶ and a polarization gate.⁷ The setting up, testing, and evaluation of experimental arrangements [**TO2, Task 4**] using both the schemes were detailed in the First Annual Report.¹ Our comparison [**TO3, Task 7**] of

the efficacy of the two schemes demonstrated that the OKG-based system provided higher temporal and spatial resolution, while the UGICS system was more user friendly, easier to implement, and provided higher signal level since the gate width was wider. It was also concluded that for breast imaging the resolution provided by the UGICS would be acceptable given the competing requirement for adequate signal level. While a narrow time gate improves the resolution, it also reduces the signal level that is crucial for forming a well-defined image. Consequently, we mainly used the UGICS-based system for time-resolved imaging experiments.

Another important experimental approach that we developed and used in the project was the *spectroscopic imaging* arrangement, also detailed in the First Annual Report.¹ The arrangement used the 1100-1300 nm light from a Cr:forsterite laser to illuminate the sample, a Fourier space gate,⁶ and a polarization gate⁷ to sort out photons that carry direct image information, and an InGaAs NIR area camera to record 2-D transillumination images. Spectroscopic imaging was an important new development in the project that was not in the original SOW, and it enabled us to explore and demonstrate the diagnostic potential of the optical imaging that was contemplated in **TO 6** and outlined in **Task 13**. Results of spectroscopic imaging were presented in earlier Annual Reports¹⁻³ and will be discussed later in this Final Report.

5.2. Time-sliced Direct Imaging of *ex vivo* Normal and Cancerous Human Breast Tissues

The efficacy of the experimental arrangements were tested and evaluated through imaging experiments on *ex vivo* human breast tissue samples (**TO 5-7, Tasks 12-17**). The samples were obtained from our collaborators at the Memorial Sloan Kettering Cancer Center (MSKCC), as well as from National Disease Research Interchange (NDRI) under Internal Review Board (IRB) approval at CCNY and were characterized by biopsy (**Task 12**) and later by pathology (**Task 17**). Breast tissue specimens from patients of different ages (between 40-70 years) and different types of breast cancers (infiltrating ductal carcinoma, infiltrating lobular carcinoma, mucinous carcinoma, invasive ductal carcinoma etc.) were investigated along with normal tissues from the same patients. The thickness of breast tissue specimens normally varied between 5-10 mm for direct imaging.

The tissue specimens were held between glass plates under compression to maintain uniform thickness and a sequence of time-sliced 2-D transillumination images were recorded for different positions of the time gate. The compression proved beneficial (**Task 13**) for maintaining uniform thickness, and avoiding voids and gaps in the specimen. Time-sliced imaging measurements of tissues with tumor (**Task 14**) demonstrated that 2-D transillumination images recorded with early arriving light highlighted the tumor, while later arriving light accentuated the normal tissue. This behavior was observed for different types of breast cancers studied in the project. Two-dimensional time-sliced images showing the difference between normal and cancerous tissues were presented in Annual Reports 1-3, and appeared in published articles⁸⁻¹¹ and presentations. Details of the experimental parameters, procedures, and results are presented in those primary sources [Reference 8 and Reference 9 are Appendix 1 and Appendix 2, respectively of First Annual Report,¹ Reference 10 is Appendix 1 of Third Annual Report,² and Reference 11 is Appendix 5 of this Final Report].

5.3. Spectroscopic Direct Imaging of *ex vivo* Normal and Cancerous Human Breast Tissues

Spectroscopic imaging experiments were carried out on the *ex vivo* breast tissue samples mentioned in Section 5.3. In most cases, time-sliced and spectroscopic imaging measurements were carried out in a coordinated manner so that the results from the two approaches could be compared. Two-dimensional transillumination images were recorded using light of several wavelengths, such as, 1210, 1225, 1235, 1250, 1280, and 1300 nm [**TO 5-7, Tasks 13 and 15**] from the Cr:forsterite laser. As a proof of principle of the diagnostic ability of spectroscopic imaging, we first carried out measurements on normal *ex vivo* breast tissues with adipose and fibrous regions.^{4,5,12} Transillumination images were recorded with light whose wavelength is close to the adipose absorption resonance¹³ at 1203 nm and compared with those recorded with off-resonance wavelength. Images recorded with near-resonant light distinguished the adipose region with higher contrast indicating the diagnostic potential of the optical imaging, if appropriate wavelengths could be identified.

While such a marked contrast was not observed between the normal and cancerous regions in the 2-D transillumination images of the breast tissue specimens, two salient features emerged. There was an overall

higher light transmission through the cancerous region at all of the above-mentioned wavelengths. What is even more interesting, a wavelength-dependent difference in light transmission through the cancerous and normal tissues was observed.^{10,11} The tumor-to-normal intensity ratio, $R_{TN}(\lambda) = I_{\text{tumor}}(\lambda)/I_{\text{normal}}(\lambda)$, where, $I_{\text{tumor}}(\lambda)$ and $I_{\text{normal}}(\lambda)$, are averaged transmitted intensities through the tumor and the normal tissue regions, respectively, had a value of 2.2 at 1225 nm, and 1.5 at 1300 nm, a significant difference.¹¹

In an alternative application involving Warthin's tumor of the parotid gland, the value of was found to be 2.9 at 1225 nm and 1.7 at 1285 nm.¹⁴ Implications of these wavelength-dependent transmission ratios are further discussed in these appended references [Reference 11 and Reference 14 are Appendix 5 and Appendix 2, respectively, of this Final Report].

5.4 Development of Analytical Solution of Radiative Transfer Equation

Development of inverse image reconstruction methods requires a theoretical model that provides an accurate description of photon transport through highly scattering turbid media. The commonly used forward model for light propagation in breast tissue is based on the Diffusion Approximation¹⁵ (DA) of the Radiative Transfer Equation (RTE). DA-based forward models cannot account for ballistic and snake photons, and lead to large errors in the region near sources, where the weight function is most important. We have made a major breakthrough in developing exact analytical solutions of the RTE and went on to build forward models based on that cumulant solution, as a part of our endeavor to develop novel inverse image reconstruction methods (TO 4, Task 10; TO 8, Task 18). Our accomplishments include the following.

- Development of an analytical solution of RTE, based on cumulant expansion, in an infinite uniform medium with an arbitrary phase function.^{16,17,18} It provides an explicit analytical expression for photon density distribution function $I(\mathbf{r}, \mathbf{s}, t)$, as a function of position \mathbf{r} , direction of light \mathbf{s} , and time t . The mean position and the half-width at half maximum height (HWHM) of the distribution are always exact. Detailed description of the approach was presented in the Second Annual Report,² and appended publication [Appendix 2 and Appendix 3 of the Second Annual Report²].
- Extension of analytical cumulant solution to include the light polarization, *i.e.*, solution of polarized photon transport equation in an infinite uniform medium that can take into account the vector nature of electromagnetic radiation and can handle the polarization property of light.¹⁹ This highly significant advance was presented in the Third Annual Report,³ and publication was appended [Appendix 2 in Third Annual Report³].
- Development of the linear cumulant forward model (CFM) based on cumulant analytical solution of the RTE.^{20,21} This CFM may be used with time-resolved, continuous-wave, and frequency-domain data to reconstruct images that are much more accurate than that provided by DA-based models. [Reference 20 and Reference 21 are Appendix 1 and Appendix 4, respectively, of this Final Report.]

5.5 Development and Demonstration of Inverse Image Reconstruction

We followed several schemes to develop and implement inverse image reconstruction (IIR) methods, (TO 4, Tasks 8, 9) and demonstrate have developed algorithms for realizing fast three-dimensional inverse image reconstruction (TO 4, Tasks 10, 11; and TO 8, Task 18). Included in the development and demonstration of IIR methods are the following.

- Development of an IIR formalism that used a point source illumination, a sequence of 2-D time-sliced images recorded with a time-gated CCD as input data, a DA-based forward model that assumes a slab geometry in cylindrical coordinates, and a Green's function perturbative approach under the Rytov approximation for obtaining a linear inversion algorithm.²² A salient feature of the formalism is the use of a 2-D matrix inversion with a 1-D Fourier transform inversion based on the cylindrical symmetry that greatly reduced the computation time. [Detailed in Appendix 3 of the First Annual Report¹]
- Development of an IIR approach based on the concept of propagation of spatial Fourier components of the scattered wave field that can use both transmitted and backscattered light from the scattering

medium containing absorbing and scattering inhomogeneities to construct 3-D images.²³ [Detailed in Appendix 4 of the Second Annual Report² and Appendix 4 of the Third Annual Report³]

Demonstration of 3-D image reconstruction based on the diffusion forward model.^{22,23} Further improvement of these inverse algorithms by combining with the forward model based on solution of RTE is being pursued.^{20,21} Details of this development appear in References 20 and 21 which are included as Appendix 1 and Appendix 4 of this Final Report, respectively.

5.6. Correlation with Existing Methods

It is imperative that any new detection and diagnostic breast imaging technology be validated by comparison with existing methods. Biopsy, x-ray, nuclear magnetic resonance (NMR), and pathology are among the commonly used methods for tumor detection and diagnosis. We have chosen breast tissue specimens for study based on biopsy results, and following optical imaging obtained histopathological evaluation of the samples (TO 5-7, Task 17) for understanding and validating results of the optical approach. Comparison with histopathology provided insight into the composition and nature of tumor and normal tissues, and helped explain observed optical results (See, for example, Reference 14 which is Appendix 2 of this Final Report).

While biopsy and pathology provide useful information for *ex vivo* specimens, alternative approaches are needed for validation of *in vivo* studies. NMR can provide an *in vivo* assessment. So, we started measurements on the same excised breast tissue specimens using both optical and NMR techniques to investigate how the results correlate (TO 5-7, Task 17) and reported the initial results in the Third Annual Report.³ We continued comparison with NMR measurements carried out at the Memorial Sloan Kettering Cancer Center by our collaborator Dr. Jason Koutcher. NMR T_1 -weighted and T_2 -weighted images of the breast tissue specimens exhibited good correlation with optical measurements. The results were presented in a major conference, and a manuscript has been submitted for publication in the conference proceedings (Appendix 5 of this Final Report). We refer to the appended manuscript for further details.

Comparison of the results from direct imaging and image reconstruction (TO 5-7, Task 16) was limited by the fact that beyond a tissue thickness of 10 mm direct imaging did not produce well resolved images, while DA-based reconstruction required thicker tissue. However, the differences observed in the direct time-sliced and spectroscopic images provided the basis for the reconstruction images to be viable.

(6) KEY RESEARCH ACCOMPLISHMENTS

- Demonstrated that time-sliced 2-D transillumination images recorded with earlier temporal slices of transmitted light highlight tumor while those recorded with later slices accentuate normal fibrous tissues in *ex vivo* human breast tissue specimens.
- Near-infrared 2-D spectroscopic imaging experiments on more breast tissue specimens could distinguish between normal adipose and fibrous tissues when transillumination images were recorded with light near resonant with the adipose absorption at 1203 nm and compared with that recorded with off-resonance light. Extending the measurements to normal and cancerous breast tissues we observe that the ratio R of light intensity transmitted through the cancerous tissue to that through the corresponding normal tissue as a function of wavelength might be used as a useful parameter for cancer identification.
- Developed analytical solutions of the scalar and vector forms of the radiative transport equation based on a cumulant expansion that enable much more accurate description of photon transport thorough scattering media than that afforded by the Diffusion Approximation. Cumulant solutions can describe all scattered photons including snake photons, and the solutions of the vector RTE can take into consideration the polarization properties of light transmitting through a highly scattering medium. Extended Cumulant Solution of scalar transport equation to semi-infinite and slab geometries making it more suited for practical application that involves finite boundaries. These analytical solutions provide basis for developing more accurate forward models and inverse image reconstruction algorithms.

- Developed an inversion algorithm that uses a temporal sequence time-sliced 2-D images as input data, a DA-based forward model and a perturbative linear inversion approach, and demonstrated fast 3-D image reconstruction.
- Developed a forward model based on the cumulant solution of the RTE for use in more sophisticated inversion algorithms for better image reconstruction of tumors in breast, and objects in obscuring media, in general.
- Demonstrated correlation between results of time-sliced optical imaging and NMR imaging methods.

(7) REPORTABLE OUTCOMES

7.1. Articles

1. S. K. Gayen and R. R. Alfano, "Sensing lesions in tissues with light," *Opt. Express* **4**, 475 (1999).
2. W. Cai, S. K. Gayen, M. Xu, M. Zevallos, M. Alrubaiee, M. Lax, and R. R. Alfano, "Optical three-dimensional inverse image reconstruction of objects in turbid media from ultrafast time-sliced optical transmission measurements," *Appl. Opt.* **38**, 4237 (1999).
3. S. K. Gayen, M. E. Zevallos, B. B. Das, and R. R. Alfano, "Near-infrared spectroscopic and time-sliced imaging of human breast tissues," *SPIE Proceedings on Optical Tomography and Spectroscopy of Tissue III* Vol. **3597**, 508 (1999).
4. M. Xu, S. K. Gayen, W. Cai, M. E. Zevallos, M. Lax, and R. R. Alfano, "Time-sliced three-dimensional inverse image reconstruction of objects in highly scattering media," *SPIE Proceedings on Optical Tomography and Spectroscopy of Tissue III* Vol. **3597**, 2 (1999).
5. M. Zevallos, S. K. Gayen, B. B. Das, M. Alrubaiee, R. R. Alfano, "Imaging of bones inside tissues using a picosecond electronic time gate," *IEEE J. Select. Topics Quantum Electron.*, **5**, 916 (1999).
6. W. Cai, M. Lax, and R. R. Alfano, "Analytical solution of the elastic Boltzmann transport equation in an infinite uniform medium using cumulant expansion," *J. Phys. Chem. B* **104**, 3996 (2000).
7. W. Cai, M. Lax, and R. R. Alfano, "Cumulant solution of the elastic Boltzmann transport equation in an infinite uniform medium," *Phys. Rev. E* **61**, 3871 (2000).
8. S. K. Gayen, M. Alrubaiee, M. E. Zevallos and R. R. Alfano, "Temporally and spectrally resolved optical imaging of normal and cancerous human breast tissues," in the *Proceedings of the Inter-Institute Workshop on In Vivo Optical Imaging at the NIH*, Amir Gandjbakhche, ed. (Optical Society of America, Washington, DC, 2000), pp. 142-147.
9. M. Xu, M. Lax, and R. R. Alfano, "Time-resolved optical diffuse tomography," *J. Opt. Soc. Am. A* **18**, 1535 (2001).
10. W. Cai, M. Lax, R. R. Alfano, "Analytical solution of the polarized photon transport equation in an infinite uniform medium using cumulant expansion," *Phys. Rev. E* **63**, 016606-1(2001).
11. M. Xu, W. Cai, M. Lax, R. R. Alfano, "Photon transport forward model for image in turbid media" *Opt. Lett.* **26** 1066-1068 (2001).
12. S. K. Gayen, M. Alrubaiee, H. E. Savage, S. P. Schantz, and R. R. Alfano, "Parotid gland tissues investigated by picosecond time-gated and spectroscopic imaging techniques," *J. Select. Topics Quantum Electron.* **7**, 906 (2001).
13. W. Cai, M. Xu, M. Lax, R. R. Alfano, "Diffusion coefficient depends on time not on absorption" *Opt. Lett.* **27** 731-733 (2002).
14. M. Xu, W. Cai, M. Lax, R. R. Alfano, "Photon migration in turbid media using a cumulant approximation to radiative transfer" *Phys. Rev. E* **65** 066609 (2002).
15. M. Al-Rubaiee, S. K. Gayen, J. A. Koutcher, and R. R. Alfano, "Cancerous and normal human tissues investigated by near-infrared time-resolved and spectroscopic imaging techniques." *SPIE Proceedings on Optical Tomography and Spectroscopy of Tissue* (to be published).

7.2. Abstracts and Presentations

1. M. Xu, S. K. Gayen, W. Cai, M. E. Zevallos, M. Lax, and R. R. Alfano, "Time-sliced three-dimensional inverse image reconstruction of objects in highly scattering media." Paper 3597-02 presented at the SPIE's International Symposium on Biomedical Optics, BIOS '99/ Photonics West, 23-29 January, San Jose, California.
2. S. K. Gayen, M. E. Zevallos, B. B. Das, and R. R. Alfano, "Near-infrared spectroscopic and time-sliced imaging of human breast tissues." Paper 3597-84 presented at the SPIE's International Symposium on Biomedical Optics, BIOS '99/ Photonics West, 23-29 January, San Jose, California.
3. S. K. Gayen, M. E. Zevallos, and R. R. Alfano, "Time-resolved transillumination imaging of normal and cancerous human breast tissues with a picosecond electronic time gate," Bull. Am. Phys. Soc. **44**, 117 (1999). Paper BC32 7 presented at the American Physical Society Centennial Meeting, March 20-26, 1999, Atlanta, Georgia.
4. S. K. Gayen, M. E. Zevallos, and R. R. Alfano, "Time-sliced and spectroscopic correlated two-dimensional near-infrared imaging for cancer detection." Paper CFL4 presented at the Conference on Lasers and Electro-Optics (CLEO'99), May 23-28, 1999, Baltimore, Maryland.
5. S. K. Gayen, M. Alrubaiee, R. R. Alfano, J. Koutcher, and H. Savage, "Electronic time-gated and spectroscopic near-infrared imaging of lesions in human tissues," Bull. Am. Phys. Soc. **45**, 958 (2000). Paper Y13 10 presented at the March Meeting of the American Physical Society, 20-24 March 2000, Minneapolis, MN.
6. S. K. Gayen, M. Alrubaiee, and R. R. Alfano, "Time-sliced and spectroscopic two-dimensional imaging of normal and cancerous human breast tissues," The Department of Defense Breast Cancer Research Program Meeting *Era of Hope*, Proceeding Volume I, p.195. Presented at the Hilton Atlanta and Towers, Atlanta, GA, June 8-11, 2000.
7. M. Xu, M. Lax, and R. R. Alfano, "Time-resolved Fourier diffuse optical tomography," in the Technical Digest of Biomedical Topical Meetings, TOPS Volume 38, Optical Society of America (2000) pp. 345-347. Paper TuC4 presented at the Biomedical Topical Meetings, Miami Beach, Florida, April 2-5, 2000.
8. W. Cai, M. Lax, and R. R. Alfano, "Analytical solution of the polarized photon transport equation in an infinite uniform scattering medium," in the Technical Digest of Biomedical Topical Meetings, TOPS Volume 38, Optical Society of America (2000) pp. 62-64. Paper TuC4 presented at the Biomedical Topical Meetings, Miami Beach, Florida, April 2-5, 2000.
9. M. Alrubaiee, S. K. Gayen, H. E. Savage, S. P. Schantz, and R. R. Alfano, "Picosecond time-gated and optical spectroscopic imaging of parotid gland tissues." Paper FP-2 presented at *Frontiers of Photonics Symposium*, City College of New York, November 5, 2001, New York.
10. M. Xu, W. Cai, M. Lax, R. R. Alfano, "Prior information and noise in three-dimensional optical image reconstruction," in the Technical Digest of OSA Biomedical Topical Meetings (2002) p30. Paper SuB7-1 presented at the Biomedical Topical Meetings, Miami Beach, Florida, April 7-10, (2002).
11. M. Xu, W. Cai, R. R. Alfano, "Three-dimensional hybrid-dual-Fourier tomography in turbid media using multiple sources and multiple detectors," Paper presented at the Third Inter-Institute Workshop on Diagnostic Optical Imaging and Spectroscopy: The Clinical Adventure on NIH campus in Bethesda, MD, Sept. 26-27 (2002).
12. W. Cai, S. K. Gayen, M. Xu, R. R. Alfano, "Improving inverse reconstruction problem for three-dimensional optical image of breast," The Department of Defense Breast Cancer Research Program Meeting *Era of Hope*, proceedings Vol III p48-1, presented at Orange County Convention Center, Orlando, Florida, Sept 25-28 (2002).
13. M. Al-Rubaiee, S. K. Gayen, W. Cai, M. Xu, J. A. Koutcher, and R. R. Alfano, "Near-infrared photonics imaging of human breast tissue." Paper P48-2 presented at *Era of Hope*, Department of Defense Breast Cancer Research Program Meeting, September 25-28, 2002, Orlando, Florida.
14. M. Al-Rubaiee, S. K. Gayen, J. A. Koutcher, and R. R. Alfano, "Cancerous and normal human tissues investigated by near-infrared time-resolved and spectroscopic imaging techniques." Paper 4955-28

presented at the Optical Tomography and Spectroscopy of Tissue V Conference of SPIE's Photonics West BIOS 2003/ Photonics West, January 25-31, 2003, San Jose, California.

7.3. Patents

1. R. R. Alfano, W. Cai, S. K. Gayen, "Time-resolved Diffusion Tomographic 2D and 3D Imaging in Highly Scattering Turbid Media" U.S. Patent 6,108,576, issued August 22, 2000.
2. R. R. Alfano, W. Cai, M. Lax, "Time-resolved optical backscattering tomographic image reconstruction in scattering turbid media" U. S. Patent 6,205,353, issued March 20, 2001.

7.4. Degrees Obtained

1. Manuel Zevallos received his Ph. D. in Electrical Engineering in 1999. Part of the research for his thesis entitled, "Near-infrared optical imaging and light propagation in highly scattering random media," was supported by this grant.
2. Min Xu received his Ph. D. in Physics in 2001. He was supported in part by this grant. The title of his thesis is, "Optical image reconstruction in highly scattering media."

7.5. Funding Applied for Based on Work Supported by this Award

1. "Two-dimensional and three-dimensional optical mammography," was submitted to USAMRMC on 6/11/02 in response to BCRP-2002.
2. "Time-resolved 2-D and 3-D imaging of breast and Prostate," submitted to the Network for Translational Research: Optical Imaging program of NCI on 2/26/03.
3. "Center for Photonic Imaging and Diagnosis of Breast Cancer," a pre-proposal submitted to USAMRMC, DoD 2003 Breast Cancer Research Program. We have recently been notified to submit a full proposal.

7.6. Research Opportunities Applied for and/or Received Based on Experience/Training Supported by this Award

Dr. Min Xu was supported in part by this grant during his doctoral work. Based on the training he received, he went on to apply for a Postdoctoral Traineeship Award. His proposal, "Time-resolved spectral optical breast tomography," was supported by USAMRMC (Grant: DAMD17-02-1-0516) for the total amount of \$150,000 covering the period of May 15, 2002- May 14, 2005.

7.7. Personnel Supported by the Research Effort **Persons Directly Supported**

1. R. R. Alfano: As the Principal Investigator (PI) of the project R. R. Alfano, Distinguished Professor of Science and Engineering, was involved in the overall supervision of the research carried out.
2. W. Cai, Research Associate: Pursued development of analytical solutions of the Radiative Transfer Equation and algorithms for inverse image reconstruction as a research associate.
3. B. B. Das, Research Associate: Supported in part by this grant, B. B. Das, was involved in the measurement of the temporal profiles of light pulses transmitted through and backscattered from breast tissues and highly scattering model media to estimate light transport parameters, such as, transport mean free path and scattering length.
4. S. K. Gayen: As a Co-PI of the project, S. K. Gayen was responsible for directing the experimental effort, and coordinating with the subcontractor, and the theoretical group. He started as a Research Associate and went on to become an Associate Professor of Physics during the period covered by the project. He was supported in part by the project.
5. X. Liang: Responsibilities included maintenance of the Ti:sapphire laser system, and help carry out imaging experiment. Received partial support as a research technician.

6. Min Xu: Min Xu was involved in the development of image reconstruction algorithms, and extension of the cumulant solution of radiative transport equation. He was supported in part as a graduate student. He received his Ph. D. and went on to earn a postdoctoral trainee grant from USAMRMC.

Persons Supported Indirectly

7. M. Alrubaiee: M. Alrubaiee is pursuing his graduate work in the area of research pursued by this project, carried out many of the project experiments. He did not receive any stipend from this effort, but the project was supported by the grant.
8. M. E. Zavallos: M. E. Zavallos received his Ph. D. in 1999, and part of his thesis work was done on this project. His stipend was derived from another source.

(8) CONCLUSIONS

The work carried out on this project provides important information about the development of time-resolved optical and spectroscopic imaging techniques for detection and diagnosis of breast cancer. *First*, direct time-sliced 2-D transillumination images can sort out tumor from normal breast tissue. Images recorded with earlier temporal slices of transmitted light highlighted cancerous tissues while those recorded with later slices accentuated normal fibrous tissues. *Second*, spectroscopic imaging shows tissue selectivity, and diagnostic potential. Wavelength dependence of a ratio, R of light intensity transmitted through the tumor and normal tissue shows the potential to be used as a useful parameter for cancer identification. *Third*, a sequence of time-sliced 2-D images provides a wealth of information for 3-D inverse image reconstruction, that are not commonly available from other optical methods. *Fourth*, analytical solutions of the scalar and vector photon transport equations using Cumulant Expansion enables more complete description of diffusive, snake and ballistic photons than the currently used methods, and can accommodate for polarization characteristics of light emerging from a scattering medium and will be useful for developing better image reconstruction approaches. *Fifth*, the theoretical formalism and computer algorithm for inverse image reconstruction scheme using both forward and backscattered light shows (with simulated data) the potential to provide fast 3-D images of scattering and absorbing objects at various depths inside a scattering medium. *Finally*, the good agreement between results of time-sliced optical measurement and NMR measurements indicates the possibility of NMR co-registration for validation of in vivo optical imaging measurements.

We plan to build on these developments and pursue *in vivo* breast imaging on volunteers following testing of the techniques on model breast structures made from excised tissues. We submitted a White Paper entitled, "Center for Photonic Imaging and Diagnosis of Breast Cancer," in response to DoD Fiscal Year 2003 Breast Cancer Research Program. We have recently been *invited to submit a full proposal*. The research programs of the envisioned Center will address the overarching question concerning early detection and diagnosis of breast cancer, and will be a natural culmination of the work carried out under this grant support.

"So What Section"

The implication of the first conclusion is that time-sliced imaging offers the possibility of highlighting cancerous lesions in human breast. The second conclusion indicates the diagnostic potential of optical imaging based upon multi-spectral measurements. X-ray mammography, most often used method, cannot diagnose cancer. The third, fourth and fifth conclusions together present the possibility of developing robust 3-D inverse image reconstruction formalisms, that in addition to being applicable for optical mammography, will be useful for imaging tumors in other body organs, such as, prostate and thyroid glands, as well as, objects inside other types of scattering media, such as, cloud, fog, smoke, and murky water. The final conclusion points to the complementary nature of optical and NMR imaging, and the possibility of using them together for better specificity. Overall, the time-sliced and spectroscopic imaging approach developed and pursued in this project may lead to the "holy grail" for obtaining breast cancer detection and diagnostic information based on wavelength selection and time-sliced image reconstruction.

(9) REFERENCES

1. Annual Report Dated September 1999 covering the period of 15 August 1998 – 14 August 1999, Award Number DAMD17-98-1-8147, on file at USAMRMC.
2. Annual Report Dated September 2000, covering the period of 15 August 1999 – 14 August 2000, Award Number DAMD17-98-1-8147, on file at USAMRMC.
3. Annual Report Dated September 2001, covering the period of 15 August 2000 – 14 August 2001, Award Number DAMD17-98-1-8147, on file at USAMRMC.
4. Q. Fu, F. Seier, S. K. Gayen, and R. R. Alfano, "A high-average-power, kilohertz- repetition-rate, sub-100-fs Ti:sapphire amplifier system," *Opt. Lett.* **22**, 712 (1997).
5. L. Wang, P. Ho, C. Liu, G. Zhang, R.R. Alfano, "Ballistic 2-D imaging through scattering walls using an ultrafast Kerr gate", *Science* **253**, 769-771 (1991).
6. J. J. Dolne, K. M. Yoo, F. Liu, and R. R. Alfano, "IR Fourier space gate and absorption imaging through random media," *Lasers Life Sci.* **6**, 131-141 (1994).
7. S. G. Demos and R. R. Alfano, "Temporal gating in highly scattering media by the degree of optical polarization," *Opt. Lett.* **21**, 161 (1996).
8. S. K. Gayen and R. R. Alfano, "Sensing lesions in tissues with light," *Opt. Express* **4**, 475 (1999).
9. S. K. Gayen, M. E. Zevallos, B. B. Das, and R. R. Alfano, "Spectroscopic and time-sliced imaging of human breast tissues," *SPIE Proceedings on Optical Tomography and Spectroscopy of Tissue III* Vol. **3597**, 508 (1999).
10. S. K. Gayen, M. Alrubaiee, M. E. Zevallos and R. R. Alfano, "Temporally and spectrally resolved optical imaging of normal and cancerous human breast tissues," in the *Proceedings of the Inter-Institute Workshop on In Vivo Optical Imaging at the NIH*, Amir Gandjbakhche, ed. (Optical Society of America, Washington, DC, 2000), pp. 142-147.
11. M. Al-Rubaiee, S. K. Gayen, J. A. Koutcher, and R. R. Alfano, "Cancerous and normal human tissues investigated by near-infrared time-resolved and spectroscopic imaging techniques." *SPIE Proceedings on Optical Tomography and Spectroscopy of Tissue* (to be published).
12. S. K. Gayen, M. E. Zevallos, and R. R. Alfano, "Near-infrared laser spectroscopic imaging: a step towards diagnostic optical imaging of human tissues," *Lasers in the Life Sciences* **8**, 187 (1999).
13. F. A. Marks, "Optical determination of the hemoglobin oxygenation state of breast biopsies and human breast cancer xenografts in nude mice," in *Proceedings of Physiological Monitoring and Early Detection Diagnostic Methods*, Thomas S. Mang and Abraham Katzir (eds.), SPIE **1641**, Bellingham, Washington, pp. 227-237, 1992.
14. S. K. Gayen, M. Alrubaiee, H. E. Savage, S. P. Schantz, and R. R. Alfano, "Parotid gland tissues investigated by picosecond time-gated and spectroscopic imaging techniques," *J. Select. Topics Quantum Electron.* **7**, 906 (2001).
15. A. Ishimaru, *Wave Propagation and Scattering in Random Media*, Vol. 1, Academic Press, 1978, pp.175-190.
16. W. Cai, M. Lax, and R. R. Alfano, "Analytical solution of the elastic Boltzmann transport equation in an infinite uniform medium using cumulant expansion," *J. Phys. Chem. B* **104**, 3996 (2000).
17. W. Cai, M. Lax, and R. R. Alfano, "Cumulant solution of the elastic Boltzmann transport equation in an infinite uniform medium," *Phys. Rev. E* **61**, 3871 (2000).
18. W. Cai, M. Xu, M. Lax, R. R. Alfano, "Diffusion coefficient depends on time not on absorption" *Opt. Lett.* **27** 731-733 (2002).

19. W. Cai, M. Lax, R. R. Alfano, "Analytical solution of the polarized photon transport equation in an infinite uniform medium using cumulant expansion," *Phys. Rev. E* **63**, 016606-1(2001).
20. M. Xu, W. Cai, M. Lax, R. R. Alfano, "Photon transport forward model for image in turbid media" *Opt. Lett.* **26** 1066-1068 (2001).
21. M. Xu, W. Cai, M. Lax, R. R. Alfano, "Photon migration in turbid media using a cumulant approximation to radiative transfer" *Phys. Rev. E* **65** 066609 (2002).
22. W. Cai, S. K. Gayen, M. Xu, M. Zevallos, M. Alrubaiee, M. Lax, and R. R. Alfano, "Optical three-dimensional inverse image reconstruction of objects in turbid media from ultrafast time-sliced optical transmission measurements," *Appl. Opt.* **38**, 4237 (1999).
23. M. Xu, M. Lax, and R. R. Alfano, "Time-resolved optical diffuse tomography," *J. Opt. Soc. Am. A* **18**, 1535 (2001).

Photon-transport forward model for imaging in turbid media

M. Xu, W. Cai, M. Lax, and R. R. Alfano

Institute for Ultrafast Spectroscopy and Lasers, New York State Center of Advanced Technology for Ultrafast Photonic Materials and Applications, and Department of Physics, The City College and Graduate Center of City University of New York, New York, New York 10031

Received February 8, 2001

A photon-transport forward model for image reconstruction in turbid media is derived that treats weak inhomogeneities through a Born approximation of the Boltzmann radiative transfer equation. This model can conveniently replace the commonly used diffusion approximation in optical tomography. An analytical expression of the background Green's function is obtained from the cumulant solution of the Boltzmann equation. Our model provides the correct behavior of photon migration at early times and reduces at long times to the center-moved diffusion approximation. Numerical comparisons between this model and the standard and center-moved diffusion models are presented. © 2001 Optical Society of America

OCIS codes: 170.6960, 290.7050, 030.5620.

Probing the internal properties of highly scattering turbid media with photons has a variety of applications in geophysics, radio astronomy, and medical tomography. Imaging based on the diffusion approximation has been pursued over the past decade because it captures the core characteristic of light migration in turbid media and is easy to implement.¹⁻³ However, in the diffusion approximation, light is assumed to diffuse from a fixed source with a constant diffusion coefficient throughout the full time range when photons propagate inside the uniform medium.⁴ This assumption is invalid when the incident photon retains its early time directionality preference. To account for this difficulty, a common practice is to assume that all the incident photons are initially scattered at a depth $z_0 = l_t$ (transport mean free path) inside the turbid medium,⁵ which we call the center-moved diffusion model (CDM). But CDM breaks the reciprocity theorem and still fails in the description of photon propagation at early times.⁶

To fully account for photon migration in a turbid medium, one must use the radiative transfer equation instead:

$$\frac{\partial}{\partial t} I(\mathbf{r}, \mathbf{s}, t) + c\mathbf{s} \cdot \nabla_{\mathbf{r}} I(\mathbf{r}, \mathbf{s}, t) + c[\mu_s(\mathbf{r}) + \mu_a(\mathbf{r})]I(\mathbf{r}, \mathbf{s}, t) = c\mu_s(\mathbf{r}) \int d\mathbf{s}' P(\mathbf{s}, \mathbf{s}') I(\mathbf{r}, \mathbf{s}', t) + q(\mathbf{r}, \mathbf{s}, t), \quad (1)$$

where $I(\mathbf{r}, \mathbf{s}, t)$ is the photon-distribution function depending on position \mathbf{r} , direction \mathbf{s} , and time t ; c is light speed inside the medium; μ_a and μ_s denote the position-dependent absorption and scattering coefficients; $q(\mathbf{r}, \mathbf{s}, t)$ is the photon-source strength; and $P(\mathbf{s}, \mathbf{s}')$ is the normalized phase function of light propagation in the medium.

Recently, we derived an analytical solution for the photon distribution, $I^{(0)}(\mathbf{r}, \mathbf{s}, t)$, and photon density, $N^{(0)}(\mathbf{r}, t)$, in an infinite uniform medium, with exact spatial center position and exact spatial half-width, at any direction and time⁷; the exact solution up to an arbitrary order of cumulants was also derived.⁸ The photon-density distribution is found to have a center that advances in time and an ellipsoidal contour that grows and changes shape, providing a clear picture

of the time evolution of light migration from the initial ballistic to the final diffusive regime. A forward model adding inhomogeneity to the analytical expression of $I^{(0)}(\mathbf{r}, \mathbf{s}, t)$ involves a complicated numerical integration over angular parameters. In this Letter we use an approximate expression of $I^{(0)}(\mathbf{r}, \mathbf{s}, t)$ that not only retains the main features of photon propagation in both early and long time limits but also is convenient for building a forward model to account for weak inhomogeneities of the medium that are treatable in the Born approximation.

The photon distribution in an infinite uniform medium, $I^{(0)}(\mathbf{r}, \mathbf{s}, t)$, is assumed to have the following form:

$$I^{(0)}(\mathbf{r}, \mathbf{s}, t | \mathbf{r}_0, \mathbf{s}_0, t_0) = N^{(0)}(\mathbf{r}, t | \mathbf{r}_0, \mathbf{s}_0, t_0) F^{(0)}(\mathbf{s}, t | \mathbf{s}_0, t_0) - \frac{3}{4\pi} D(t - t_0) \mathbf{s} \cdot \nabla_{\mathbf{r}} N^{(0)}(\mathbf{r}, t | \mathbf{r}_0, \mathbf{s}_0, t_0), \quad (2)$$

where $N^{(0)}(\mathbf{r}, t | \mathbf{r}_0, \mathbf{s}_0, t_0)$ is the photon density for a point pulse propagating along \mathbf{s}_0 at position \mathbf{r}_0 and time t_0 in an infinite uniform medium, $F^{(0)}(\mathbf{s}, t | \mathbf{s}_0, t_0)$ is the known exact photon distribution in light-direction space, and $D(t - t_0)$ is the time-dependent diffusion coefficient. The full definitions of these quantities originated in Ref. 7 and are given as follows: $F^{(0)}(\mathbf{s}, t | \mathbf{s}_0, t_0) = (4\pi)^{-1} \sum_l (2l + 1) \exp[-g_l(t - t_0)] P_l(\mathbf{s} \cdot \mathbf{s}_0)$, where $g_l = c\mu_s[1 - a_l/(2l + 1)]$, a_l are the coefficients in the Legendre expansion of the phase function, $P(\mathbf{s}, \mathbf{s}') = (4\pi)^{-1} \sum_l a_l P_l(\mathbf{s} \cdot \mathbf{s}')$, especially, $g_0 = 0$ and $g_1 = c\mu_s'$, where μ_s' is the reduced scattering coefficient. The diffusion coefficient $D(t)$ is taken to be an average of the time-dependent semimajor axis, D_{zz} , and semiminor axes $D_{xx} = D_{yy}$ of the diffusion coefficient ellipsoid:

$$D(t) = \frac{D_{xx} + D_{yy} + D_{zz}}{3} = \frac{c}{3t} \left\{ \frac{t}{g_1} - \frac{1 - \exp(-g_1 t)}{g_1^2} - \frac{[1 - \exp(-g_1 t)]^2}{2g_1^2} \right\}. \quad (3)$$

The photon density is given by

$$N^{(0)}(\mathbf{r}, t | \mathbf{r}_0, \mathbf{s}_0, t_0) = \frac{1}{[4\pi D(t - t_0)c(t - t_0)]^{3/2}} \times \exp\left\{-\frac{[\mathbf{r} - \mathbf{r}_0 - \mathbf{s}_0\Delta(t - t_0)]^2}{4D(t - t_0)c(t - t_0)}\right\} \exp[-\mu_a c(t - t_0)], \quad (4)$$

where $\Delta(t) = c[1 - \exp(-g_1 t)]/g_1$ is the average center of photons, which moves with speed c initially and stops at $c/g_1 = l_t$ in the long time limit.

At the early times $t \rightarrow t_0$, the first term of Eq. (2) dominates, and $F^{(0)}(\mathbf{s}, t | \mathbf{s}_0, t_0) \rightarrow \delta(\mathbf{s} - \mathbf{s}_0)$, $D(t - t_0) \rightarrow c^2(t - t_0)^2 \mu_s'/9 \rightarrow 0$, and $N^{(0)}(\mathbf{r}, t | \mathbf{r}_0, \mathbf{s}_0, t_0) \rightarrow \delta[\mathbf{r} - \mathbf{r}_0 - c(t - t_0)\mathbf{s}_0]$; thus $I^{(0)}(\mathbf{r}, \mathbf{s}, t | \mathbf{r}_0, \mathbf{s}_0, t_0)$ provides a correct picture of ballistic motion at the speed of light along the incident direction, \mathbf{s}_0 . In the long time limit, $F^{(0)}(\mathbf{s}, t | \mathbf{s}_0, t_0) \rightarrow (4\pi)^{-1}$, $D(t) \rightarrow (3\mu_s')^{-1}$, Eq. (2) reduces to the photon distribution of the CDM approximation.

A perturbative method is then used to obtain the forward model when weak inhomogeneities are introduced into the otherwise uniform medium. Making a perturbation expansion of the radiative transfer equation (1) to the first-order Born approximation, we derive the change in photon distribution from $I^{(0)}(\mathbf{r}, \mathbf{s}, t)$, which is the photon distribution of the uniform background, as

$$\begin{aligned} \delta I(\mathbf{r}, \mathbf{s}, t | \mathbf{r}_0, \mathbf{s}_0, t_0) &= \int dt' \int d\mathbf{r}' \int d\mathbf{s}' I^{(0)}(\mathbf{r}', -\mathbf{s}', t - t' | \mathbf{r}, -\mathbf{s}) \\ &\times \left\{ \int d\mathbf{s}'' c \delta[\mu_s P](\mathbf{s}', \mathbf{s}'', \mathbf{r}') I^{(0)}(\mathbf{r}', \mathbf{s}'', t - t_0 | \mathbf{r}_0, \mathbf{s}_0) \right. \\ &\left. - c[\delta\mu_s(\mathbf{r}') + \delta\mu_a(\mathbf{r}')] I^{(0)}(\mathbf{r}', \mathbf{s}', t' - t_0 | \mathbf{r}_0, \mathbf{s}_0) \right\}, \quad (5) \end{aligned}$$

where $\delta\mu_a$, $\delta\mu_s$, and $\delta[\mu_s P]$ are the changes of the absorption coefficient, the scattering coefficient, and the angular-dependent differential scattering coefficient, respectively, from the background to the inhomogeneity. The optical reciprocity theorem, $I^{(0)}(\mathbf{r}, \mathbf{s}, t - t' | \mathbf{r}', \mathbf{s}') = I^{(0)}(\mathbf{r}', -\mathbf{s}', t - t' | \mathbf{r}, -\mathbf{s})$, is used to obtain Eq. (5).

Expanding $\delta[\mu_s P]$ in Legendre polynomials and substituting Eq. (2) into Eq. (5), the integrations over angular variables in Eq. (5) can be analytically performed. We obtain

$$\begin{aligned} \delta I(\mathbf{r}, \mathbf{s}, t | \mathbf{r}_0, \mathbf{s}_0, t_0) &= -\frac{1}{4\pi} \int dt' \int d\mathbf{r}' c \delta\mu_a(\mathbf{r}') \\ &\times N^{(0)}(\mathbf{r}', t - t' | \mathbf{r}, -\mathbf{s}) N^{(0)}(\mathbf{r}', t - t_0 | \mathbf{r}_0, \mathbf{s}_0) \\ &+ \frac{3c}{4\pi} \int dt' \int d\mathbf{r}' D(t - t') D(t' - t_0) [\delta\mu_a(\mathbf{r}') + \delta\mu_s'(\mathbf{r}')] \\ &\times \nabla_{\mathbf{r}'} N^{(0)}(\mathbf{r}', t - t' | \mathbf{r}, -\mathbf{s}) \cdot \nabla_{\mathbf{r}'} N^{(0)}(\mathbf{r}', t' - t_0 | \mathbf{r}_0, \mathbf{s}_0) \\ &+ \frac{3c}{4\pi} \int dt' \int d\mathbf{r}' D(t - t') [\delta\mu_a(\mathbf{r}') + \delta\mu_s'(\mathbf{r}')] \exp(-g_1 t') \\ &\times \{N^{(0)}(\mathbf{r}', t - t_0 | \mathbf{r}, -\mathbf{s}) \mathbf{s} \cdot \nabla_{\mathbf{r}'} N^{(0)}(\mathbf{r}', t - t' | \mathbf{r}_0, \mathbf{s}_0) \\ &- \mathbf{s}_0 \cdot \nabla_{\mathbf{r}'} N^{(0)}(\mathbf{r}', t - t' | \mathbf{r}, -\mathbf{s}) N^{(0)}(\mathbf{r}', t' - t_0 | \mathbf{r}_0, \mathbf{s}_0)\} \quad (6) \end{aligned}$$

after neglecting fast-decaying terms involving $\exp(-2g_1 t)$ for $l \geq 1$.

The photon-transport forward model (PTFM), Eq. (6), is the main result in this Letter and obeys the reciprocal relation $\delta I(\mathbf{r}, \mathbf{s}, t - t_0 | \mathbf{r}_0, \mathbf{s}_0) = \delta I(\mathbf{r}_0, -\mathbf{s}_0, t - t_0 | \mathbf{r}, -\mathbf{s})$. In the long time limit, the term in Eq. (6) that contains the exponential decay factor $\exp(-g_1 t')$ can be neglected, and the change in photon density, $4\pi \delta I(\mathbf{r}, \mathbf{s}, t)$ in the PTFM, is reduced to the diffuse imaging model [Eq. (14) in Ref. 9].

To show the difference between our model and the diffusion models, we consider a point photon pulse $\delta(\mathbf{r})\delta(\mathbf{s} - \hat{z})\delta(t)$ propagating inside an infinite scattering turbid medium with absorption coefficient $\mu_a = 0$, reduced scattering coefficient $\mu_s' = 1 \text{ mm}^{-1}$, anisotropy $g = 0.9$, and refractive index $n = 1.33$. These optical properties are similar to those of a typical breast tissue. A Henyey-Greenstein phase function is adopted in the following calculations.¹⁰

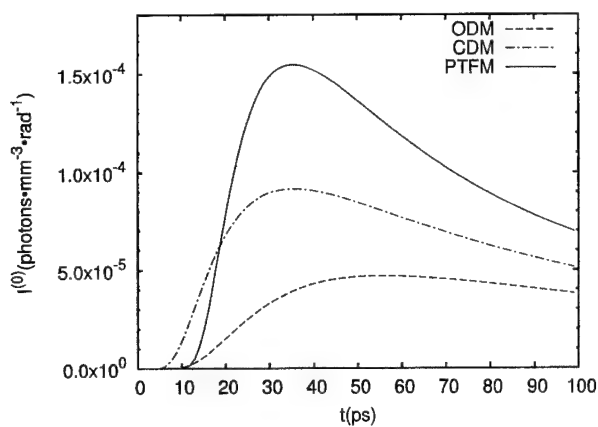
The time-resolved profiles of transmission $I^{(0)}(\mathbf{r}, \hat{z}, t)$ at position $\mathbf{r} = (0, 0, 5) \text{ mm}$ and backscattering $I^{(0)}(\mathbf{r}, -\hat{z}, t)$ at position $\mathbf{r} = (0, 2, 0) \text{ mm}$ are shown by the solid curves in Figs. 1(a) and 1(b), respectively. For comparison, the photon density divided by 4π from the original diffusion model (ODM) and the CDM are also plotted.

In a transmission case [Fig. 1(a)], the peak photon intensity in the ODM arrives too late compared with the experimental result reported by Yoo *et al.*,¹¹ whereas in the CDM the artificial adjustment of the source position for l_t leads to an arrival of photons faster than light speed. The intensity at forward directions from our model is stronger than that of diffusion models, which indicates that a certain anisotropic angular distribution remains even at a distance of $5l_t$ from the source.

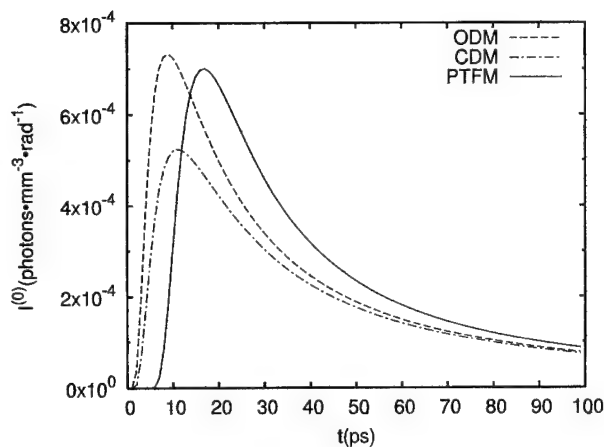
In the case of backscattering [Fig. 1(b)], photons diffuse from the origin $(0, 0, 0)$ to $(0, 2, 0) \text{ mm}$ with a constant diffusion coefficient $D = l_t/3$ in the ODM, whereas photons diffuse from the adjusted source position $(0, 0, 1) \text{ mm}$ to $(0, 2, 0) \text{ mm}$ with the same constant diffusion coefficient in the CDM. The photons in our model are backscattered to $(0, 2, 0) \text{ mm}$ later than those in the ODM and the CDM because the center of photons moves forward along the positive z direction and diffuses from the moving center with a gradually increasing diffusion coefficient from 0 to $l_t/3$ in the PTFM.

Consider a forward model with a scattering inhomogeneity $\delta\mu_s' = 0.1 \text{ mm}^{-1}$ of unit volume placed at position $(0, 0, 2) \text{ mm}$. The time-resolved profiles of $-\delta I(\mathbf{r}, \hat{z}, t)$ at position $\mathbf{r} = (0, 0, 5) \text{ mm}$ and $\delta I(\mathbf{r}, -\hat{z}, t)$ at position $\mathbf{r} = (0, 2, 0) \text{ mm}$ from Eq. (6) and those from diffusion models are shown in Fig. 2. The significant difference between our model and diffusion models shows that the nondiffusive nature of photon migration at early times is important and cannot be neglected when the separation of any pair of source, inhomogeneity, and detector is small.

In conclusion, a photon-transport forward model of image reconstruction in turbid media has been derived by use of the Born approximation of the radiative transfer equation. A simplified cumulant solution in an



(a)



(b)

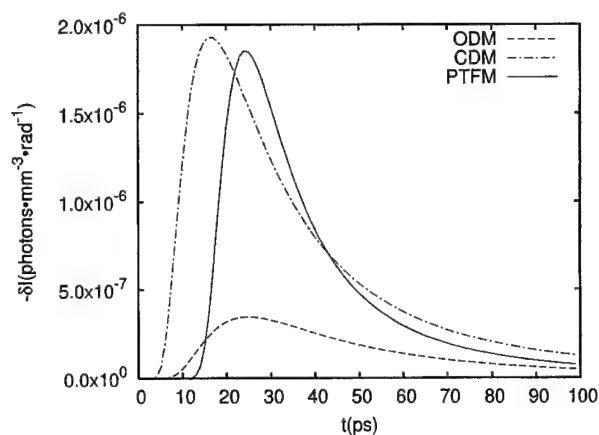
Fig. 1. Photon-distribution profiles (a) $I^{(0)}(\mathbf{r}, \hat{z}, t)$ at position $\mathbf{r} = (0, 0, 5)$ mm and (b) $I^{(0)}(\mathbf{r}, -\hat{z}, t)$ at position $\mathbf{r} = (0, 2, 0)$ mm.

infinite uniform medium serves as the background Green's function. This model provides a correct picture of nearly ballistic motion of photons at early times and reduces to the center-moved diffusion approximation at long times. Extension to semi-infinite and slab geometries of this model is being studied.

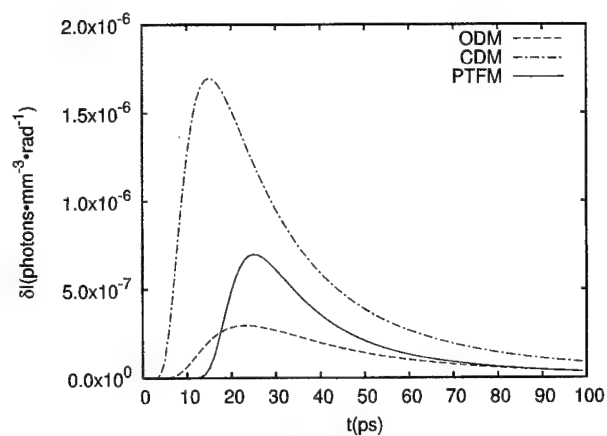
This research was supported in part by Center for Laser Imaging and Cancer Diagnostics (Grant 47997003). M. Xu's e-mail address is minxu@sci.ccnycun.edu.

References

1. R. R. Alfano, S. G. Demos, and S. K. Gayen, *Ann. N.Y. Acad. Sci.* **820**, 248 (1997).
2. A. G. Yodh, B. Tromberg, E. Sevick-Muraca, and D. Pine, eds., feature on Diffusing Photons in Turbid Media *J. Opt. Soc. Am. A* **14**, 136–342 (1997).
3. S. R. Arridge and J. C. Hebden, *Phys. Med. Biol.* **42**, 841 (1997).
4. K. Furutsu and Y. Yamada, *Phys. Rev. E* **50**, 3634 (1994).
5. M. S. Patterson, B. Chance, and B. C. Wilson, *Appl. Opt.* **28**, 2331 (1989).
6. Y. Tsuchiya, K. Ohta, and T. Urakami, *Jpn. J. Appl. Phys. Part 1* **34**, 2495 (1995).
7. W. Cai, M. Lax, and R. R. Alfano, *Phys. Rev. E* **61**, 3871 (2000).
8. W. Cai, M. Lax, and R. R. Alfano, *J. Phys. Chem. B* **104**, 3996 (2000).
9. S. R. Arridge, *Appl. Opt.* **34**, 7395 (1995).
10. L. G. Henyey and J. L. Greenstein, *Astrophys. J.* **93**, 70 (1941).
11. K. M. Yoo, F. Liu, and R. R. Alfano, *Phys. Rev. Lett.* **64**, 2647 (1990).



(a)



(b)

Fig. 2. Changes of photon-distribution function (a) $-\delta I(\mathbf{r}, \hat{z}, t)$ at position $\mathbf{r} = (0, 0, 5)$ mm and (b) $\delta I(\mathbf{r}, -\hat{z}, t)$ at position $\mathbf{r} = (0, 2, 0)$ mm.

Parotid Gland Tissues Investigated by Picosecond Time-Gated and Optical Spectroscopic Imaging Techniques

S. K. Gayen, Mohammad Alrubaiee, Howard E. Savage, Stimson P. Schantz, and R. R. Alfano, *Fellow, IEEE*

Abstract—Near-infrared (NIR) time-resolved and spectroscopic transillumination imaging techniques are used to investigate normal tissues and Warthin's tumor of human parotid glands. The time-sliced imaging arrangement uses 120-fs, 1-kHz repetition-rate, 800-nm pulses from a Ti:sapphire laser and amplifier system for sample illumination and an ultrafast gated intensified camera system (UGICS) for recording two-dimensional (2-D) images using transmitted light. Images recorded with earlier temporal slices (approximately first 100 ps) of transmitted light highlight the tumor, while those recorded with later temporal slices (later than 200 ps) accentuate normal tissues. The spectroscopic imaging arrangement uses 1210–1300 nm tunable output of a Cr:forsterite laser for sample illumination, a Fourier space gate to discriminate against multiple-scattered light, and a NIR area camera to record 2-D images. The tumor region in the specimen appears brighter than the normal region in spectroscopic images recorded with light of different wavelengths. A wavelength-dependent variation in the ratio of light transmission through the tumor to that through the normal parotid gland is observed. Differences in scattering and wavelength-dependent absorption characteristics of normal parotid gland and Warthin's tumor provide a consistent explanation of these observed features. Histopathological analysis of the specimen sheds light on the probable origin of the differences in scattering and absorption characteristics.

Index Terms—Near-infrared imaging, optical biomedical imaging, parotid gland, photon propagation in highly scattering media, time-gated imaging, transillumination imaging, Warthin's tumor.

I. INTRODUCTION

OPTICAL biomedical imaging techniques are attracting interest as promising noninvasive means for detection and diagnosis of tumors and abnormalities in human body [1]–[11]. Body organs that are potentially amenable to optical imaging investigation include breast, brain, gastro-intestinal tract, obstetric and gynecological tract, prostate, skin, salivary glands, arteries, and bones. Development of appropriate and effective optical modalities for *in vivo* clinical imaging of lesions in any of these

organs is an involved process. An important step in this development process is testing of the efficacy of the method on *ex vivo* tissue specimens of the target organ, which in turn provides key information about light transport and optical spectroscopic characteristics of the types of tissues under investigation. We have initiated such a study of *ex vivo* normal and abnormal tissues from different organs using a variety of near-infrared (NIR) optical imaging techniques. In this paper, we present results of time-sliced and spectroscopic two-dimensional (2-D) NIR imaging experiments on excised normal tissues and Warthin's tumor of the parotid gland.

Time-sliced imaging [6], [10], [12] is an extension of the concept of time-resolved early-light imaging [13]–[17] wherein a sequence of 2-D images of the sample under investigation is recorded using different temporal slices of light emergent from the sample, in addition to the early-arriving part. Differences in light transport properties of constituent tissues in a sample are highlighted in the 2-D images obtained with different temporal slices of the transmitted light. We use ultrashort pulses of light from a femtosecond Ti:sapphire laser to illuminate the sample and a time-gated camera with a variable gate position to record 2-D images with the gated fraction of the forward transmitted light.

Spectroscopic imaging [18] uses light of different colors to exploit any spectroscopic difference for enhancing image contrast and exploring diagnostic potential. In a spectroscopic imaging measurement, one uses light of different wavelengths to record 2-D transillumination images of the sample under investigation. If a part of the sample happens to have a different response to light at a particular wavelength than the rest, then "resonant" (or "near-resonant") images recorded with light of that wavelength (or a wavelength near the resonance) provide contrast between that part and rest of the sample [18]. Comparisons with "nonresonant" images that are obtained using light of wavelengths away from the resonance help accentuate the contrast even further.

The parotid glands, located in the tissue inferior and anterior to the ears, are the largest of the three main pairs of salivary glands [19]. They secrete the serous (thin, watery) component of the saliva, and the parotid duct delivers the secretion into the mouth. Diseases of the parotid glands include Warthin's tumor (*cystadenoma lymphomatosum*) [20], and pleomorphic adenoma. In this article, we present results of optical imaging experiments on an *ex vivo* tissue specimen with normal parotid gland tissue and Warthin's tumor. Warthin's tumor is the second most common benign tumor that accounts for 5% to 10% of

Manuscript received April 9, 2001. This work was supported in part by US-AMRMC, DOE, and the NASA IRA Program.

S. K. Gayen, M. Alrubaiee, and R. R. Alfano are with the Institute for Ultrafast Spectroscopy and Lasers, New York State Center for Advanced Technology for Ultrafast Photonic Materials and Applications, Department of Physics, The City College of the City University New York, New York, NY 10031 USA.

H. E. Savage and S. P. Schantz are with the New York Eye and Ear Infirmary, New York, NY 10003 USA and also with Strang Cancer Prevention Center, New York, NY 10021 USA.

Publisher Item Identifier S 1077-260X(01)11189-5.

all parotid gland tumors. The tumor commonly is a round to oval encapsulated mass 1 cm to 10 cm in diameter with a characteristic lymphoid component. It is located in the parotid or preauricular lymph nodes in 99% of the cases [21], [22]. The cut surface of the tumor is gray in color and has cystic or cleftlike spaces filled with a gray or light brown mucinous secretion. Tall columnar cells that overlie lymphoid tissue line the cystic or cleft like spaces.

The remainder of the article is organized as follows. Section II presents an outline of the experimental methods, and a brief description of the samples used in the experiment. Section III presents optical imaging results along with histopathological analysis of the samples. In Section IV, we discuss the implications of the experimental results.

II. EXPERIMENTAL METHODS

A. Time-Sliced Imaging

Experimental arrangement for time-sliced imaging, shown schematically in Fig. 1(a), made use of approximately 120-fs duration, 1-kHz repetition-rate pulses from a Ti:sapphire laser and amplifier system [23] for sample illumination, and an ultrafast gated intensified camera system (UGICS) for recording 2-D images using picosecond-duration slices of light transmitted through the sample. The laser output was tunable over the 750–850 nm spectral range with an average power of 3 W. We used approximately 200 mW at 800 nm for experiments reported here. A beam expander expanded the beam and an aperture selected a 3-cm diameter central part of it to illuminate the sample.

The UGICS was a compact time-gated image intensifier unit that was fiber-optically coupled to a charge-coupled device (CCD) camera. It provided an electronic time gate whose FWHM duration could be adjusted to a minimum of approximately 80 ps. The temporal position of the gate could be electronically varied over a 20-ns range with a minimum step size of 25 ps. The CCD camera had a 384×286 pixels sensing element with a pixel size of $23 \mu\text{m} \times 23 \mu\text{m}$. A 24-mm focal-length $f/2.8$ camera lens collected the signal transmitted through the tissue sample and directed it to the sensing element. The transillumination signal recorded by the UGICS at a particular gate position was a convolution of the transmitted light pulse with the gate pulse centered on the gate position. A personal computer stored and displayed the resulting 2-D images.

B. Spectroscopic Imaging

The experimental arrangement for near-infrared (NIR) spectroscopic imaging, displayed in Fig. 1(b), used the 1210–1300 nm continuous-wave mode-locked output of a Cr^{4+} :forsterite laser to illuminate the sample. A set of calibrated neutral density filters helped maintain the average optical power of the incident beam at approximately 35 mW for all the wavelengths used in the imaging experiment. A beam expander expanded the beam and an aperture selected a 3-cm diameter central part of it to illuminate the sample.

A Fourier space gate [24] selected out a fraction of the less-scattered image-bearing photons from the strong background

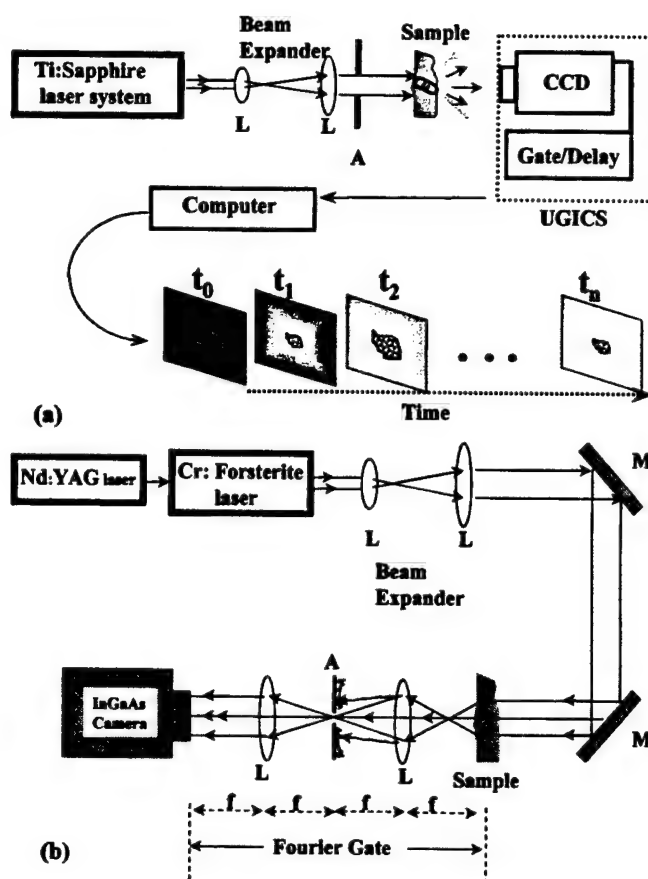


Fig. 1. Schematic diagram of the experimental arrangement for: (a) time-sliced imaging and (b) spectroscopic imaging. Key: A = aperture, L = lens, M = mirror, CCD = charge-coupled device, UGICS = ultrafast gated intensified camera system.

of the image-blurring diffuse photons. A 50 mm focal-length camera lens placed on the optical axis at a distance of 50 mm from the aperture in the Fourier gate collected and collimated the low-spatial-frequency light filtered by the aperture and directed it to the 128×128 pixels sensing element of an InGaAs near-infrared (NIR) area camera.

C. Sample

Excised parotid gland tissue specimen used in the experiments reported in this article was obtained from the New York Eye and Ear Infirmary (NYEEI) under Internal Review Board approvals at the City College of New York and NYEEI. The specimen came from the left parotid gland of a 37-year-old male patient. It was a gray/brown nodule surrounded by normal salivary gland parenchyma. The nodule itself was focally cystic with a papillary appearance. The clinical diagnosis was a benign Warthin's tumor of the left parotid gland.

The specimen was received on ice. It was held between two glass plates and slightly compressed to ensure same overall thickness for optical imaging measurements. The dimensions of this slightly compressed sample were $20 \text{ mm} \times 10 \text{ mm} \times 5 \text{ mm}$. Light transited through the 5 mm path length of the sample for transillumination imaging measurements reported here. After NIR imaging experiments, the sample was placed in formalin and transferred to NYEEI for histological analysis.

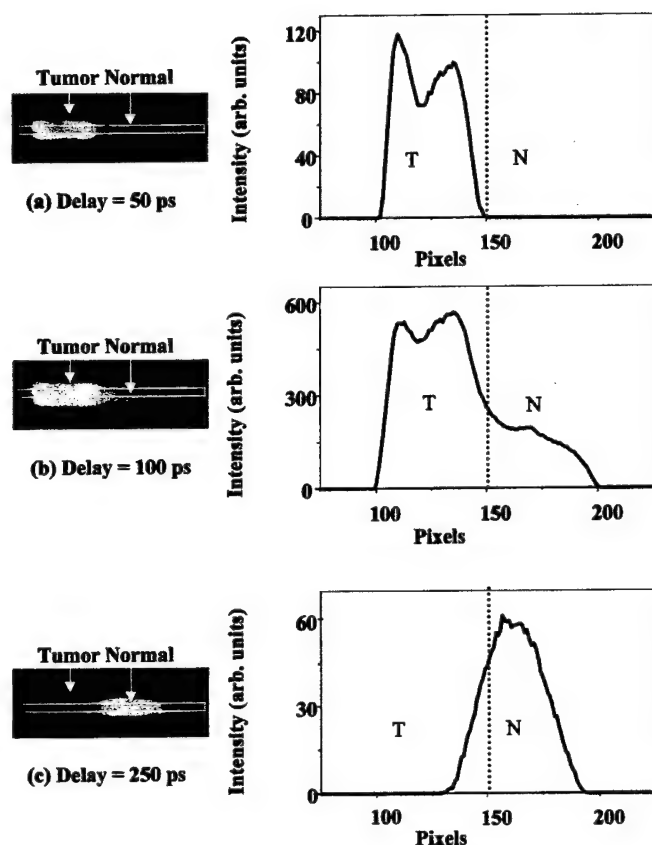


Fig. 2. Time-sliced 2-D images (left frames) of a 20 mm \times 10 mm \times 5 mm parotid gland tissue sample with normal parotid gland (N) and Warthin's tumor (T) for gate positions of (a) 50 ps, (b) 100 ps, and (c) 250 ps. Corresponding spatial intensity profiles integrated over the same horizontal area highlighted by white dashed boxes in the images are shown in the right side frames. The zero position was taken to be the time of arrival of the light pulse through a 5-mm-thick quartz cell filled with water.

III. RESULTS

A. Time-Sliced Imaging

Time-sliced 2-D transillumination images of the parotid gland sample for gate positions of 50 ps, 100 ps, and 250 ps are displayed in the left frames of Fig. 2(a)–(c), respectively. The zero position was taken to be the time of arrival of the light pulse through a 5-mm-thick quartz cell filled with water. The corresponding frames to the right present the spatial intensity profiles of the respective images integrated over the same horizontal area in all the figures. The salient feature of the images is the differences in time-dependent brightness of the normal tissue and Warthin's tumor in the sample. In the early 50-ps image of Fig. 2(a) only the tumor is visible. The corresponding horizontal spatial profile exhibits peak in the tumor region and hits the baseline in the normal tissue region. At this early time, markedly more light is transmitted through the tumor than the normal parotid gland tissue. With time the image of normal parotid gland tissue gains in brightness and the corresponding region of the spatial profile rises above the baseline, as the typical sampling of Fig. 2(b) for the delay position of 100 ps shows. At later times (250 ps) the image of the normal gland becomes brighter than the tumor, the corresponding spatial

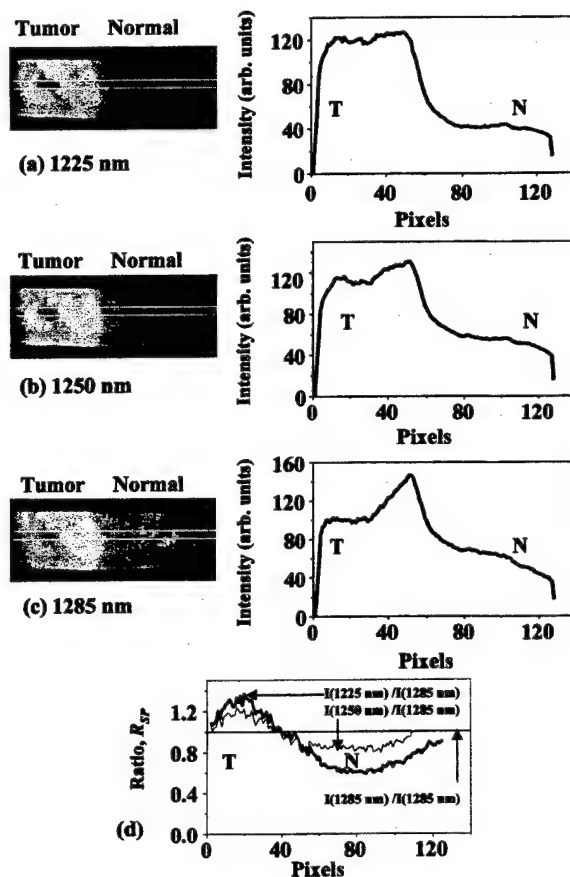


Fig. 3. Spectroscopic 2-D images (left frames) of the parotid gland tissue sample with normal parotid gland (N) and Warthin's tumor (T) for light of wavelengths (a) 1225 nm, (b) 1250 nm, and (c) 1285 nm. Corresponding spatial intensity profiles integrated over the same horizontal area highlighted by white dashed boxes in the images are shown in the right frames. No time gating was used. (d) Spatial profiles of the ratio of intensities $R_{SP}(\lambda)$, as described in the text, for the reference wavelength of 1285 nm, and probing wavelengths of 1225 and 1250 nm.

profile peaks in the normal gland position indicating higher light transmission through the normal gland than the tumor [Fig. 2(c)].

These results indicate that light transits faster through Warthin's tumor than normal parotid gland tissue. Lower scattering or/and higher absorption of light by the tumor may account for the observed temporal behavior. Since there is no known absorption of 800-nm light by parotid gland tissues, we attribute these time-dependent differences in the relative light transmission through Warthin's tumor and normal parotid gland tissues to the differences in the light scattering characteristics of these components of tissues.

B. Spectroscopic Imaging

Spectroscopic images of the specimen recorded using light of wavelengths 1225, 1250, and 1285 nm appear in the left side frames of Fig. 3(a)–(c), respectively. Corresponding spatial profiles integrated over the same horizontal area in all the images appear in the right side frames. The salient feature of the images is the higher brightness of the Warthin's tumor region compared to the normal parotid gland region for all three wavelengths.

Since no time gating is used in spectroscopic imaging, the result is indicative of higher overall light transmission through the tumor than that through the normal parotid gland.

Another subtle feature is the wavelength dependence of relative light transmission through the tumor and the normal tissue. We examined the variation in relative brightness with wavelength by monitoring the tumor-to-normal intensity ratio, $R_{TN}(\lambda) = I_{\text{tumor}}(\lambda)/I_{\text{normal}}(\lambda)$, where $I_{\text{tumor}}(\lambda)$ and $I_{\text{normal}}(\lambda)$ are the averaged intensities through the Warthin's tumor and normal parotid gland regions, respectively, of the spatial profile at wavelength λ . The values of $R_{TN}(\lambda)$ for 1225, 1250, and 1285 nm are 2.9, 2.0, and 1.7, respectively.

Even more instructive is the ratio of intensities $R_{SP}(\lambda) = I(\lambda)/I(\lambda_R)$, where $I(\lambda)$ and $I(\lambda_R)$ are the values of intensities at probing wavelength λ and selected reference wavelength λ_R , respectively, measured at the same location in the respective images. The horizontal spatial profiles of $R_{SP}(\lambda)$ for $\lambda_R = 1285$ nm and $\lambda = 1225$ and 1250 nm averaged over the width of the dashed lines in the images of Fig. 3(a)–(c) are shown in Fig. 3(d). These profiles were obtained by taking the ratio of spatial profile at wavelength λ to that at 1285 nm. The salient feature of the $R_{SP}(\lambda)$ profiles in Fig. 3(d) is that the tumor region tends to have a higher value of the ratio (>1) than the normal region (<1).

The transition region between the Warthin's tumor and normal parotid gland appears brighter than the rest of the tumor in the spectroscopic images and the corresponding spatial intensity profiles tend to peak around pixel 50. The peak is more prominent in the spatial profile of Fig. 3(c) than in other profiles. A histological examination of the specimen revealed that although this region was composed of the same lymphoid and epithelial elements as the rest of the tumor, the tissue in this area was less dense and had more lymphoid tissue than epithelial tissue compared to the rest of the tumor. These differences lead to higher light transmission through the transition region. This result indicates the sensitivity of spectroscopic imaging to variations in tissue density and morphology.

IV. DISCUSSION

The results of both the time-sliced imaging and spectroscopic imaging experiments show the ability of the two techniques to select between the Warthin's tumor and normal parotid gland tissues. The contrast between the Warthin's tumor and the normal parotid gland is most dramatic in the images recorded with earlier and later time slices. We observed similar contrast between normal and cancerous regions in the time-sliced images of human breast tissue specimens as well [6], [25].

Spectroscopic images exhibit three main features: (a) overall higher light transmission through the tumor; (b) a wavelength-dependent variation in tumor-to-normal intensity ratio, $R_{TN}(\lambda)$; and (c) a variation in the spatial profile of the ratio, $R_{SP}(\lambda)$ between the tumor and normal regions of a specimen. We attribute the higher light transmission through the Warthin's tumor compared to that through the normal parotid gland at all three wavelengths to lower light scattering by the tumor. This attribution is consistent with the results of the time-sliced imaging experiment carried out with 800-nm femtosecond

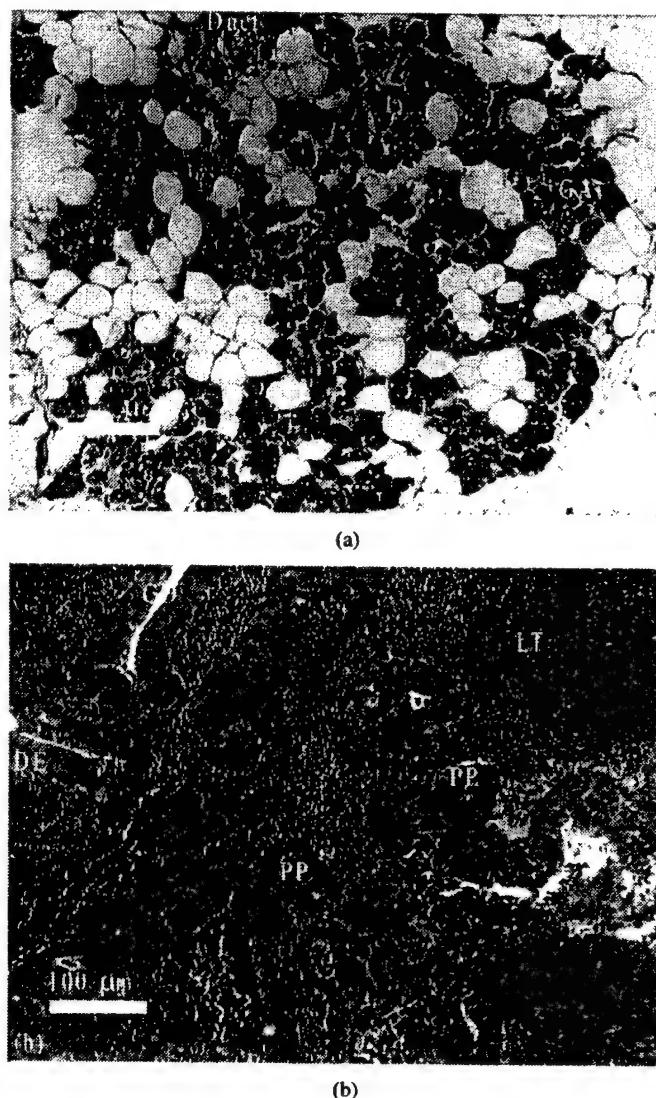


Fig. 4. Histological micrograph of a representative section from: (a) the normal parotid gland used in the optical imaging experiment showing fat cells (FC), glandular alveoli (GA), and ducts (Duct) and (b) the Warthin's tumor showing double layers (columnar and cuboidal) of ductal epithelium (DE), clefts of the duct (CD), papillary projections (PP) of the ductal epithelium, cystic spaces (CS), and areas of lymphoid tissue (LT).

light pulses. The wavelength dependent variation in $R_{TN}(\lambda)$ and $R_{SP}(\lambda)$ is expected to be associated with difference in absorption by the normal parotid gland and tumor.

In order to obtain a better appreciation of the origin of the differences in scattering and absorption characteristics of normal parotid gland and Warthin's tumor, we turned to the histopathological analysis of the sample. Histopathology provides detailed information about the structural differences between the normal and abnormal tissues and sets the standard against which the performance of any new technique should be evaluated.

Fig. 4(a) presents a histological micrograph of a representative section of the normal parotid gland tissue used in the optical imaging experiment. The key features are the fat cells (FC), glandular alveoli (GA), and ducts (Duct). Fig. 4(b) is a micrograph of a similar representative section from the Warthin's tumor in the specimen under same magnification. The features in the histology of the Warthin's tumor are double layers (columnar and cuboidal) of ductal epithelium (DE),

clefts of the duct (CD), papillary projections (PP) of the ductal epithelium, cystic spaces (CS), and areas of lymphoid tissue (LT). The contrast with the histology of the normal parotid gland is quite distinct.

Light scattering depends on the size, shape, and relative refractive indices of the scattering entities. The aforementioned structural differences between the tumor and normal parotid gland are likely to lead to different light scattering and spectroscopic characteristics. A quantitative evaluation of the role of different scatterers is highly involved that will require independent measurement of the optical and scattering characteristics of each of the different scattering entities, and modeling of their distribution in the tissue ultrastructure.

A particularly significant difference observed in the micrographs of the two representative sections that has important consequences for NIR imaging experiments is the paucity of fat (adipose) cells in the Warthin's tumor, and their abundance in the normal parotid gland. Two characteristics of adipose tissues may shed light on the observed results of NIR imaging experiments. First, adipose tissues scatter light more effectively than other types of tissues, such as, fibrous, glandular, and ductal [6], [25], [26]. Second, adipose tissue has a broad optical absorption band centered on 1203 nm [26]. The histological analysis shows that the normal parotid gland tissue has a much higher abundance of adipose cells than that in Warthin's tumor. Light transiting through the normal tissue will be more scattered by the adipose cells, traverse longer distance within the sample, and arrive later in time than that transiting through the Warthin's tumor. It thus provides an explanation of the results of time-sliced imaging experiments that show early-light images highlighting the tumor, while the late-light images accentuate the normal parotid gland.

The results of spectroscopic imaging arrangement may be explained as well. The normal part of the sample appears darker in the spectroscopic images Fig. 3(a)–(c) as the more abundant adipose cells there contribute to higher scattering (more loss of light) than the tissues in the tumor. Adipose cells in the normal parotid gland are one of the major contributors to the scattering, but may not be the sole reason for higher scattering by normal tissue.

The light wavelength of 1225 nm is closer to the adipose absorption peak at 1203 nm, 1250 nm is in the wing of the absorption band, while 1285 nm is away from the absorption resonance. Consequently, among the three wavelengths presented in Fig. 3(a)–(c), 1225-nm light is absorbed the most by the adipose cells in the normal part of the specimen, 1285-nm light the least, with the 1250-nm light in between. This wavelength-dependent absorption contributes to the observed decrease in the ratio between 1225 nm to 1285 nm. The tumor-to-normal ratio $R_{TN}(\lambda)$ thus acts as a parameter to differentiate between normal tissue and Warthin's tumor of the parotid gland. The use of this ratio for *in vivo* application requires knowledge of the suspect region and a normal region, and evaluation of the ratio between transmitted intensities through the abnormal to normal region.

The ratio $R_{SP}(\lambda)$ is a more promising parameter since it involves measurements of two intensities, one at a reference wavelength and the other at a wavelength near-resonant with adipose absorption, at the same location and evaluation of the ratio. In

obtaining the spatial profiles of $R_{SP}(\lambda)$ displayed in Fig. 3(d), we used 1285 nm that is far-removed from the adipose resonance peak at 1203 nm as the reference wavelength, and 1225 and 1250 nm that lie within the adipose optical absorption band as probing wavelengths. We obtain a higher contrast between the tumor and normal regions in the $R_{SP}(\lambda)$ profile that uses intensities at 1225 nm, the wavelength closer to the resonance peak. However, in both the $R_{SP}(\lambda)$ profiles using 1225 nm and 1250 nm, the ratio values tend to be more than one for the tumor region, and less than 1 for the normal region. Assuming that this trend holds, a measurement of $R_{SP}(\lambda)$ value at a location in the specimen may identify it as either tumor ($R_{SP} > 1$) or normal ($R_{SP} < 1$), and no comparison with another region is needed. More measurements on a larger number of samples with different stages of tumor progression will be needed to build up statistics for establishing the values of parameters R_{SP} and R_{TN} that will be indicative of the status of tissue (tumor or normal) with requisite specificity.

In summary, the results of these experiments further demonstrate the potential of NIR time-sliced and spectroscopic imaging techniques for detection and diagnosis of tumors in optically accessible suspect body organs.

ACKNOWLEDGMENT

The authors acknowledge M. Zevallos, A. Katz, and J. Evans for technical help, and S. McCormick for a helpful discussion.

REFERENCES

- [1] G. J. Muller, R. R. Alfano, S. R. Arridge, J. Beuthan, E. Gratton, M. Kaschke, B. R. Masters, S. Svanberg, and P. van der Zee, Eds., *Medical Optical Tomography: Functional Imaging and Monitoring*. ser. SPIE Institute Series. Bellingham, WA: SPIE, 1993, vol. IS 11.
- [2] S. K. Gayen and R. R. Alfano, "Emerging optical biomedical imaging techniques," *Opt. Photon. News*, vol. 7, no. 3, pp. 17–22, 1996.
- [3] D. Grosenick, H. Wabnitz, H. Rinneberg, K. T. Moesta, and P. Schlag, "Development of a time-domain optical mammography system and first *in vivo* applications," *Appl. Opt.*, vol. 38, pp. 2927–2943, 1999.
- [4] M. A. Francheschini, K. T. Moesta, S. Fantini, G. Gaida, E. Gratton, H. Hess, W. W. Mantulin, M. Seeber, P. M. Schlag, and M. Kaschke, "Frequency-domain techniques enhance optical mammography: Initial clinical results," *Proc. Natl. Acad. Sci. USA*, vol. 94, pp. 6468–6473, 1997.
- [5] S. A. Boppart, B. E. Bouma, C. Pitris, J. F. Southern, M. E. Brezinski, and J. G. Fujimoto, "In vivo cellular optical coherence tomography imaging," *Nature Med.*, vol. 4, pp. 861–864, 1998.
- [6] S. K. Gayen and R. R. Alfano, "Sensing lesions in tissues with light," *Opt. Express*, vol. 4, pp. 475–480, 1999.
- [7] J. C. Hebden, S. R. Arridge, and D. T. Depty, "Optical imaging in medicine: I. Experimental techniques," *Phys. Med. Biol.*, vol. 42, pp. 841–853, 1997.
- [8] B. Chance, M. Cope, E. Gratton, N. Ramanujam, and B. Tromberg, "Phase measurement of light absorption and scatter in human tissues," *Rev. Sci. Instrum.*, vol. 69, pp. 3457–3481, 1998.
- [9] T. O. McBride, B. W. Pogue, E. Gerety, S. Poplack, U. L. Osterberg, and K. D. Paulsen, "Spectroscopic diffuse optical tomography for quantitatively assessing hemoglobin concentration and oxygenation in tissue," *Appl. Opt.*, vol. 38, pp. 5480–5490, 1999.
- [10] M. E. Zevallos, S. K. Gayen, B. B. Das, M. Alrubaiee, and R. R. Alfano, "Picosecond electronic time-gated imaging of bones in tissues," *IEEE J. Select. Topics Quantum Electron.*, vol. 5, pp. 916–922, July/Aug. 1999.
- [11] H. Eda, I. Oda, Y. Ito, Y. Wada, Y. Oikawa, Y. Tsunazawa, M. Takada, Y. Tsuchiya, Y. Yamashita, A. Sassarolli, Y. Yamada, and M. Tamura, "Multichannel time-resolved tomographic imaging system," *Rev. Sci. Instrum.*, vol. 70, pp. 3593–3602, 1999.
- [12] W. Cai, S. K. Gayen, M. Xu, M. Zevallos, M. Alrubaiee, M. Lax, and R. R. Alfano, "Optical tomographic image reconstruction from ultrafast time-sliced transmission measurements," *Appl. Opt.*, vol. 38, pp. 4237–4246, 1999.

- [13] K. M. Yoo and R. R. Alfano, "Time-resolved coherent and incoherent components of forward light scattering in random media," *Opt. Lett.*, vol. 15, pp. 320-322, 1990.
- [14] R. R. Alfano, X. Linag, L. Wang, and P. Ho, "Time-resolved imaging of translucent droplets in highly scattering media," *Science*, vol. 264, pp. 1913-1915, 1994.
- [15] L. Wang, P. P. Ho, G. Liu, G. Zhang, and R. R. Alfano, "Ballistic 2-D imaging through scattering walls using an ultrafast optical Kerr Gate," *Science*, vol. 253, pp. 769-771, 1991.
- [16] M. S. Patterson, B. Chance, and B. C. Wilson, "Time-resolved reflectance and transmittance for the noninvasive measurement of tissue optical properties," *Appl. Opt.*, vol. 28, pp. 2331-2336, 1989.
- [17] B. B. Das, K. M. Yoo, and R. R. Alfano, "Ultrafast time gated imaging in thick tissues: A step toward optical mammography," *Opt. Lett.*, vol. 18, pp. 1092-1094, 1993.
- [18] S. K. Gayen, M. E. Zevallos, M. Alrubaiee, and R. R. Alfano, "Near-infrared laser spectroscopic imaging: A step toward diagnostic optical imaging of human tissues," *Laser Life Sci.*, vol. 8, pp. 187-198, 1999.
- [19] E. P. Solomon and P. W. Davis, *Human Anatomy and Physiology*. Philadelphia, PA: CBS, 1983.
- [20] A. S. Warthin, "Papillary cystadenoma lymphomatosum," *J. Cancer Res.*, vol. 13, pp. 116-125, 1929.
- [21] J. W. Eveson and R. A. Cawson, "Warthin's tumor (cystadenolymphoma) of salivary glands: A clinicopathologic investigation of 278 cases," *Oral Surg. Oral Med. Oral Pathol.*, vol. 61, pp. 256-262, 1986.
- [22] J. Lamelas, J. H. Terry, and A. E. Alfonso, "Warthin's tumor: Multicentricity and increasing incidence in women," *Amer. J. Surg.*, vol. 154, pp. 347-351, 1987.
- [23] Q. Fu, F. Seier, S. K. Gayen, and R. R. Alfano, "High-average-power kilohertz-repetition-rate sub-100-fs Ti:sapphire amplifier system," *Opt. Lett.*, vol. 22, pp. 712-714, 1997.
- [24] J. J. Dolne, K. M. Yoo, F. Liu, and R. R. Alfano, "IR Fourier space gate and absorption imaging through random media," *Laser Life Sci.*, vol. 6, pp. 131-141, 1994.
- [25] S. K. Gayen, M. Alrubaiee, M. E. Zevallos, and R. R. Alfano, "Temporally and spectrally resolved optical imaging of normal and cancerous human breast tissues," in *Proc. Inter-Institute Workshop on In Vivo Optical Imaging at the NIH*, A. H. Gandjebakhche, Ed., Washington, DC, 2000, pp. 142-147.
- [26] F. A. Marks, "Optical determination of the hemoglobin oxygenation state of breast biopsies and human breast cancer xenografts in nude mice," in *Proc. Physiological Monitoring and Early Detection Diagnostic Methods*, T. S. Mang and A. Katzir, Eds., Bellingham, WA, 1992, pp. 227-237.



S. K. Gayen received the B.Sc.(Hons.) and M.Sc. degrees in physics from the University of Dacca, Bangladesh, and the Ph.D. degree in physics from the University of Connecticut, Storrs.

He is currently an Associate Professor of physics at the City College of New York and affiliated with the New York State Center for Advanced Technology for Ultrafast Photonics, City University of New York. His research interests are in optical biomedical imaging, tunable solid-state lasers, spectroscopy of impurity ions in solids, nonlinear optics, and

ultrafast laser spectroscopy. He has published over 50 articles and holds three U.S. patents.

Dr. Gayen is a member of the American Physical Society and the Optical Society of America.



Mohammad Alrubaiee received his B.S. degree in electrical engineering in 1993 from the City College of the City University of New York. He is currently a graduate student in the Department of Physics and a research assistant at the Institute for Ultrafast Spectroscopy and Lasers, the City College of New York. His graduate research involves time-resolved and optical spectroscopic imaging of biomedical media.

He has published four articles in refereed journals.



Howard E. Savage received the B.S. and M.S. degrees from the University of Vermont, Burlington, and the Ph.D. degree in microbiology from Rutgers University, New Brunswick, NJ.

He received his postdoctoral training at Baylor College of Medicine, Waco, TX, and joined the faculty as and Instructor in the Division of Oncology, Department of Pharmacology. He was Research Associate with the Department of Head and Neck Surgery, M.D. Anderson Cancer Center, University of Texas, Austin. He joined the Head and Neck

Research Service, Department of Surgery at Memorial Sloan-Kettering Cancer Center, New York, as Attending Cell Biologist and Memorial Hospital, New York, as an Assistant Laboratory Member. Currently, he has three affiliations: the New York Medical College as an Assistant Professor, The New York Eye and Ear Infirmary, Department of Pathology, as a Cell Biologist, and The Strang Cancer Prevention Clinic, New York, as an adjunct Research Scientist. Among his research interests are the use of optics to detect and follow molecular transitions in human cells and tissue.



Stimson P. Schantz graduated from the College of Medicine, University of Cincinnati, Cincinnati, OH, in 1975.

He is a Professor of Otolaryngology and Head, Division of Head and Neck Surgery, New York Medical College, and Head of the Department of Otolaryngology/Head and Neck Surgery, New York Eye and Ear Infirmary, New York. He is actively involved in both laboratory and clinical research and received numerous grants for conducting research on the biology and treatment of head and neck cancer. His current re-

search interests are in the areas of genetic susceptibility, novel screening strategies, chemoprevention and biologic therapy for head and neck cancer, as well as, laser imaging in cancer diagnostics. He has published over 150 articles in peer-reviewed journals and textbooks.

Dr. Schantz is a member, and has served as director of many prestigious societies and committees. Most recently, in collaboration with international colleagues, he has founded the International Institute for Head and Neck Cancer and Tobacco-Related Diseases. He has received many honors and awards during his career, the most recent being the Harris F. Mosher Award for outstanding clinical research from the Triologic Society in 1997.



R. R. Alfano (M'87-SM'89-F'01) is a Distinguished Professor of Science and Engineering with the City College of the City University of New York, and Director of the Institute for Ultrafast Spectroscopy and Lasers, the New York State Center for Advanced Technology for Ultrafast Photonics, and the Center for Laser Imaging and Cancer Diagnostics, a Department of Energy Center of Excellence at the City College of New York. His research has encompassed a wide variety of areas including optical biomedical imaging, photon

propagation through turbid media, ultrafast laser science and technology, ultrafast supercontinuum generation, tunable solid-state lasers, nonlinear optics, as well as dynamical processes in semiconductors, dielectric crystals, molecular systems, polymers, and biological systems. He has published over 600 papers, edited four books on ultrafast laser science and applications, organized several major conferences, and holds 81 patents.

Dr. Alfano is a fellow of the American Physical Society and the Optical Society of America.

Diffusion coefficient depends on time, not on absorption

Wei Cai, M. Xu, Melvin Lax, and R. R. Alfano

Institute for Ultrafast Spectroscopy and Lasers, New York State Center of Advanced Technology for Ultrafast Photonic Materials and Applications, Department of Physics, The City College and Graduate Center of City University of New York, New York, New York 10031

Received November 27, 2001

The recent controversy over whether the photon diffusion coefficient depends on absorption is addressed by use of the analytical solution of the photon transport equation in an infinite homogeneous scattering medium. The diffusion coefficient is found to be independent of absorption but temporally dependent. After a long period of time, the photon diffusion coefficient approaches $D = 1/3\mu_s'$, which supports a claim made by Furutsu and Yamada [Phys. Rev. E **50**, 3634 (1994)]. At early times, the diffusion coefficient is smaller than $D = 1/3\mu_s'$, but this reduction cannot be expressed as $D = 1/3(\mu_s' + \mu_a)$, since the time-dependent diffusion coefficient is found to be unrelated to absorption. © 2002 Optical Society of America

OCIS codes: 290.1990, 030.5620, 170.5280, 290.7050.

The diffusion approximation of the radiative transfer equation has been used extensively in the study of photon migration and applications in turbid media. A controversy exists about the form of diffusion coefficient D in media in coexistence with scattering and absorption. In traditional derivations of the diffusion equation from the transport equation, the diffusion coefficient is obtained as¹⁻⁴

$$D = 1/3(\mu_s' + \mu_a), \quad (1)$$

where μ_s' is the reduced scattering coefficient and μ_a is the absorption coefficient. Furutsu and Yamada⁵ and Furutsu⁶ pointed out that this form of D does not consist of the transformation property of the transport equation in an infinite homogeneous turbid medium: the photon distribution function at position \mathbf{r} , in direction \mathbf{s} and time t , $I(\mathbf{r}, \mathbf{s}, t) = \exp(-c\mu_a t)I_0(\mathbf{r}, \mathbf{s}, t)$, where $I_0(\mathbf{r}, \mathbf{s}, t)$ is the solution for the same medium but without absorption. They^{5,6} suggested another derivation that leads to

$$D = l_t/3 = 1/3\mu_s', \quad (2)$$

which is independent of absorption, where l_t is the transport mean-free path. This claim has been supported by Bassani *et al.*,⁷ Durduran *et al.*,⁸ and Nakai *et al.*⁹ based on experiments and Monte Carlo simulations. In contrast, in later papers Aronson and Corngold,¹⁰ Rinzeima *et al.*,¹¹ and Durian¹², based on their experiments and numerical simulations, asserted that D should depend on absorption.

Most recently, we developed an analytical solution of the transport equation in an infinite homogeneous medium.^{13,14} We derived¹⁴ an expression for the spatial cumulants of the photon distribution function $I(\mathbf{r}, \mathbf{s}, t)$ at any direction \mathbf{s} and time t , exact up to an arbitrarily high cumulant order, which can be used for accurate computation of the photon distribution function. Up to the second cumulant order, we obtained an approximate Gaussian spatial distribution that has the exact central position and the exact half-width of the distribution.¹³ For photon density $N(\mathbf{r}, t)$,

at $t \rightarrow \infty$ our result approaches the center-moved diffusion approximation (CMDA), with $D = 1/3\mu_s'$ independent of absorption. At a finite time, the diffusion coefficient D increased from zero at $t = 0$ to the above value at $t \rightarrow \infty$. Typically, in the case of the anisotropic factor $g \sim 0.9$ it takes approximately $10l_t$ for the diffusion mode to be valid, as shown experimentally by Yoo *et al.*¹⁵ This $D(t)$ as a function of time is determined only by scattering parameters unrelated to absorption. Hence, it is physically unreasonable to use Eq. (1) to reduce the value of D at a finite time to fit experimental or simulated data.

The time-dependent photon density $N(\mathbf{r}, t)$ obtained from the CMDA in an infinite homogeneous medium for a collimated pulse source located at $\mathbf{r} = 0$ with incident direction along $\hat{\mathbf{z}}$ is given by¹⁶

$$N(\mathbf{r}, t) = \frac{1}{(4\pi Dct)^{3/2}} \exp\left[-\frac{(\mathbf{r} - l_t\hat{\mathbf{z}})^2}{4Dct} - \mu_a ct\right], \quad (3)$$

where D is the diffusion constant. This solution differs from the standard diffusion solution in that the center of the distribution is moved by l_t from the source position along the incident direction. On the other hand, our cumulant approximation (CUMA) for photon density, exact up to the second-order cumulant from the same source, is obtained as^{13,14}

$$N(\mathbf{r}, t) = \frac{1}{(4\pi D_{zz}ct)^{1/2}} \frac{1}{4\pi D_{xx}ct} \exp\left[-\frac{(z - R_z)^2}{4D_{zz}ct}\right] \times \exp\left[-\frac{(x^2 + y^2)}{4D_{xx}ct}\right] \exp(-\mu_a ct), \quad (4)$$

with the moving center located at

$$R_z = c[1 - \exp(-g_1 t)]/g_1. \quad (5)$$

The corresponding diffusion coefficients are given by

$$D_{zz} = \frac{c}{3t} \left\{ \frac{t}{g_1} - \frac{3g_1 - g_2}{g_1^2(g_1 - g_2)} [1 - \exp(-g_1 t)] \right. \\ \left. + \frac{2}{g_2(g_1 - g_2)} [1 - \exp(-g_2 t)] \right. \\ \left. - \frac{3}{2g_1^2} [1 - \exp(-g_1 t)]^2 \right\}, \quad (6)$$

$$D_{xx} = D_{yy} = \frac{c}{3t} \left\{ \frac{t}{g_1} + \frac{g_2}{g_1^2(g_1 - g_2)} [1 - \exp(-g_1 t)] \right. \\ \left. - \frac{1}{g_2(g_1 - g_2)} [1 - \exp(-g_2 t)] \right\}. \quad (7)$$

Here $g_l = \mu_s c [1 - a_l / (2l + 1)]$, where the single-scattering phase function is expanded in Legendre polynomials by

$$P(\cos \theta) = [1/(4\pi)] \sum_l a_l P_l(\cos \theta).$$

Two special values of g_l are $g_0 = 0$ and $g_1 = c/l_t$.

The original meaning of diffusion is a description of a random process. As early as when Brownian motion was first studied, researchers have known that under random forces from the surrounding medium particles will take a diffusion process, namely, spread from the center outward. The diffusion coefficient is a parameter that characterizes the rate of spread, which can be time dependent. The standard diffusion equation with a diffusion constant is the simplest form with which to describe these phenomena. The photon propagation in a turbid medium is one example of the random processes, which is more complicated than that described by the standard diffusion equation, mainly because the photons are injected with velocity along a direction. This leads to photon propagation from ballistic to snakelike and then to the diffusive mode. The diffusion coefficient in this process should be time dependent.

The fundamental time-independent parameters of the medium are the scattering coefficients, the absorption coefficients, and the phase function in the radiative transfer equation, because they have definite meaning from a microscopic viewpoint. When regarding the diffusion constant as a physical parameter, we should note that this concept is not original but is a secondary quantity that is derived by use of an approximate method. Of course, these two meanings of a diffusion coefficient are not incompatible. When a standard diffusion equation is approximately valid, the diffusion constant is correct according to both meanings.

Although the Gaussian distribution in Eq. (4) is an approximation because it cuts into the second-order cumulant, Eqs. (6) and (7) provide an exact description of the half-width of the real distribution.

Figure 1 shows the diffusion coefficients from CUMA, D_{zz} and D_{xx} [Eqs. (6) and (7)], as a function of time, where g_l are calculated by Mie theory¹⁷ assuming (for this figure) that the homogeneous scattering medium consists of water droplets with $\rho/\lambda = 1$ uniformly distributed in air, with ρ the radius of the droplet, λ the wavelength of light, and index of refraction $m = 1.33$. The anisotropic factor for this case is $a_1/3 = 0.8436$.

At $t \rightarrow \infty$, the photon density in Eq. (4) approaches Eq. (3), where the diffusion coefficients D_{zz} and D_{xx} approach $D = 1/3\mu_s'$, not Eq. (1). This means that Eq. (1) for a diffusion coefficient that depends on absorption leads to an incorrect result even for an infinite time limit. On the other hand, the central-limit theorem claims that the obtained Gaussian distribution would be accurate after a large number of collisions. Hence, Eq. (3) with $D = 1/3\mu_s'$ provides an accurate solution of photon transport in an infinite homogeneous medium at an infinite time limit, no matter whether absorption is strong or weak. At finite times, the diffusion coefficient is always smaller than its value at infinite time. In fact, at early time $t \rightarrow 0$, the center moves as $ct\hat{z}$ and the diffusion coefficient approaches zero. This result presents a clear picture of nearly ballistic motion at $t \rightarrow 0$. With an increase in time, the motion at the center slows down, and the diffusion coefficient increases from zero. This stage of photon migration is in the snakelike mode. For a large period of time, Eq. (4) approaches the center-moved diffusion solution. As shown in Eqs. (6) and (7), the time-dependent diffusion coefficient is determined only by the scattering parameters g_l and is unrelated to the absorption coefficient μ_a . Hence, to fit data of numerical simulation or experiments at finite time, one should not use Eq. (1) to reduce the diffusion coefficient.

The Aronson and Corngold paper¹⁰ emphasizes that the time-independent diffusion equation rather than the time-dependent equation should be examined to determine which form of diffusion coefficient is correct. The time-independent solution can be obtained by integration of the time-dependent solution over time. Integration of Eq. (3) over time yields the time-independent diffusive solution in an infinite homogeneous medium:

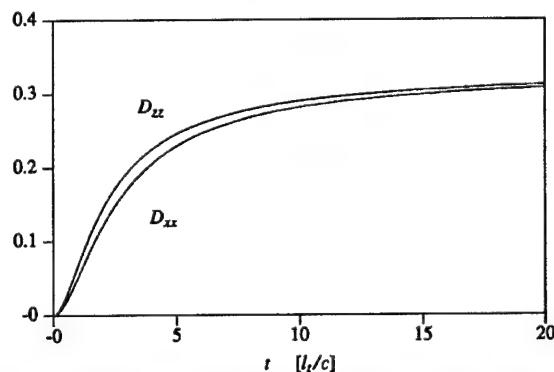


Fig. 1. Diffusion coefficients D_{zz} and D_{xx} from Eqs. (6) and (7) as a function of time t .

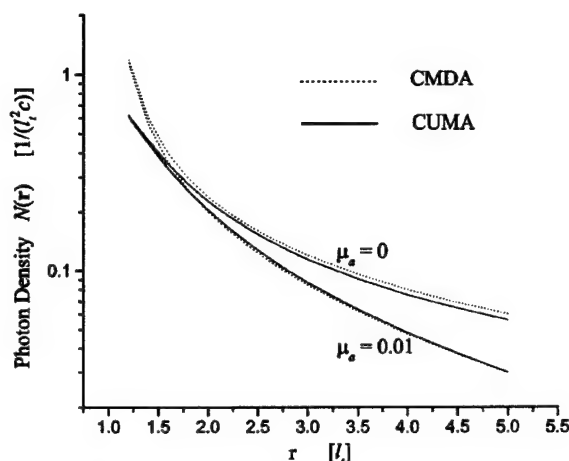


Fig. 2. Steady-state photon density as a function of distance from the source (along the incident direction) for different absorption coefficients μ_a with unit $1/l_t$ obtained with the CMDA and the CUMA. The unit of length is l_t ; the unit of time is l_t/c .

$$N(\mathbf{r}) = \frac{1}{4\pi Dc|\mathbf{r} - l_t \hat{\mathbf{z}}|} \exp[-|\mathbf{r} - l_t \hat{\mathbf{z}}|(\mu_a/D)^{1/2}]. \quad (8)$$

A more accurate steady-state distribution $N(\mathbf{r})$ in an infinite homogeneous medium can be obtained by integration of Eq. (4) over time from $t = 0$ to $t = \infty$. Figure 2 shows $N(\mathbf{r})$ as a function of r with the detector set at $(0, 0, r)$ for different absorption coefficients μ_a . The dashed curves were obtained from Eq. (8) with $D = l_t/3$, and the solid curves were obtained by integration of our time-dependent cumulant solution in Eq. (4) over time, with the corresponding diffusion coefficients given by Eqs. (6) and (7). When the detector is near the source, the photon density from CUMA is distinctly smaller than that from Eq. (8). This happens because early time photons play an important role, and the diffusion approximation fails when it is near the source. With an increase in distance between source and detector, the results from the CMDA and CUMA approaches are in agreement for different absorption coefficients. These results confirm that the diffusion

coefficient should be $D = l_t/3$ at the diffusion limit, independently of absorption.

In conclusion, our analytical solution of the time-dependent photon density in an infinite homogeneous medium supports the claim that the diffusion coefficients is independent of absorption but is temporally dependent.

This research is supported in part by NASA Institutional Research Awards, U.S. Army Medical Research and Materiel Command, the U.S. Army Research Office, the U.S. Department of Energy, and the Defense Advanced Research Projects Agency.

References

1. A. Ishimaru, *Wave Propagation and Scattering in Random Media* (Academic, New York, 1978), Vol. 1.
2. S. Glasstone and M. C. Edlund, *The Elements of Nuclear Reactor Theory* (Van Nostrand, New York, 1952).
3. W. M. Star, J. P. Marijnissen, and M. J. C. van Gemert, *Phys. Med. Biol.* **33**, 437 (1988).
4. J. J. Duderstadt and W. R. Martin, *Transport Theory* (Wiley, New York, 1979).
5. K. Furutsu and Y. Yamada, *Phys. Rev. E* **50**, 3634 (1994).
6. K. Furutsu, *J. Opt. Soc. Am. A* **14**, 267 (1997).
7. M. Bassani, F. Martelli, G. Zaccanti, and D. Contini, *Opt. Lett.* **22**, 853 (1997).
8. T. Durduran, A. G. Yodh, B. Chance, and D. A. Boas, *J. Opt. Soc. Am. A* **14**, 3358 (1997).
9. T. Nakai, G. Nishimura, K. Yamamoto, and M. Tamura, *Phys. Med. Biol.* **42**, 2541 (1997).
10. R. Aronson and N. Corngold, *J. Opt. Soc. Am. A* **16**, 1066 (1999).
11. K. Rinzema, L. H. P. Murrer, and W. M. Star, *J. Opt. Soc. Am. A* **15**, 2078 (1998).
12. D. J. Durian, *Opt. Lett.* **23**, 1502 (1998).
13. W. Cai, M. Lax, and R. R. Alfano, *Phys. Rev. E* **61**, 3871 (2000).
14. W. Cai, M. Lax, and R. R. Alfano, *J. Phys. Chem. B* **104**, 3996 (2000).
15. K. M. Yoo, F. Liu, and R. R. Alfano, *Phys. Rev. Lett.* **64**, 2647 (1990).
16. M. S. Patterson, B. Chance, and B. C. Wilson, *Appl. Opt.* **28**, 2331 (1995).
17. C. F. Bohren and D. R. Huffman, *Absorption and Scattering of Light by Small Particles* (Wiley, New York, 1983).

Photon migration in turbid media using a cumulant approximation to radiative transfer

M. Xu,* W. Cai, M. Lax, and R. R. Alfano

Institute for Ultrafast Spectroscopy and Lasers, New York State Center of Advanced Technology for Ultrafast Photonics and Department of Physics, The City College and Graduate Center of City University of New York, New York, New York 10031

(Received 1 August 2001; published 18 June 2002)

A photon transport model for light migration in turbid media based on a cumulant approximation to radiative transfer is presented for image reconstruction inside an infinite medium or a bounded medium with a planar geometry. This model treats weak inhomogeneities through a Born approximation of the Boltzmann radiative transfer equation and uses the second-order cumulant solution of photon density to the Boltzmann equation as the Green's function for the uniform background. It provides the correct behavior of photon migration at early times and reduces at long times to the center-moved diffusion approximation. At early times, it agrees much better with the result from the Monte Carlo simulation than the diffusion approximation. Both approximations agree well with the Monte Carlo simulation at later times. The weight function for image reconstruction under this proposed model is shown to have a strong dependence at both early and later times on absorption and/or scattering inhomogeneities located in the propagation direction of and close to the source, or in the field of view of and close to the detector. This effect originates from the initial ballistic motion of incident photons, which is substantially underestimated by the diffusion approximation.

DOI: 10.1103/PhysRevE.65.066609

PACS number(s): 42.25.Dd, 05.60.Cd, 42.30.Wb, 02.70.Uu

I. INTRODUCTION

Photon migration in turbid media is a random walk in which rays or photons traverse a medium of scatterers and absorbers, and undergo multiple scattering and absorption events before escaping. A natural framework to deal with this type of problem is provided by the theory of radiative transfer in Chandrasekhar's classic text [1]. The linear Boltzmann equation governs the radiation field in a medium that absorbs, emits, and scatters radiation [2]. Because the Boltzmann equation is a nonseparable, integro-differential equation of first order for which an exact closed-form solution is not known except for a few special cases, various approximations have been devised [1,3,4]. The most common approximation is the diffusion approximation, which corresponds to the lowest-order truncation in the spherical harmonic expansion of the photon distribution function. It follows from the Boltzmann equation under the assumption that the photon distribution is almost isotropic after a sufficient large number of scattering events, and thus provides an asymptotic approximation applicable to later times [5]. The diffusion approximation is invalid when the incident photon still retains its directionality preference. Moreover, approximations using higher-order truncation in the spherical harmonic expansion of the photon distribution function are still inefficient in describing the ballistic movement of photons at early times [6]. Yoo *et al.* [7] reported that the diffusion approximation fails for small and intermediate scattering ranges. The range of failure is proportional to the transport mean free path $l_t = l_s / (1 - g)$ where l_s is the scattering mean free path and g is the scattering anisotropy (the average cosine of the scattering angle). For one important class of applications of photon migration in a turbid medium—the medical applications, the medium has a strongly peaked phase function in the forward direction and a typical trans-

port mean free path $l_t \sim 1$ mm for human breast tissue. The diffusion approximation is thus incorrect for a substantial scattering range. In optical tomography [8–13] where the distribution of inhomogeneities inside a highly scattering medium is reconstructed from measurements of the transmitted light surrounding the medium, the diffusion approximation yields a much underestimated weight function when any separation between the source, the inhomogeneity, and the detector is small. This error may distort the signal from the inhomogeneity inside the medium because the weight function near surface is usually much larger than that inside.

Recently, an analytical solution to the Boltzmann equation was derived by the authors in an infinite uniform medium using a cumulant expansion [14,15]. An exact but formal solution to the Boltzmann equation yields the photon distribution function $I(\mathbf{r}, \mathbf{s}, t)$ at position \mathbf{r} , direction \mathbf{s} , and time t ,

$$I(\mathbf{r}, \mathbf{s}, t) = \left\langle \delta \left[\mathbf{r} - \mathbf{c} \int_0^t \mathbf{s}(t') dt' \right] \delta(\mathbf{s}(t) - \mathbf{s}) \right\rangle, \quad (1)$$

for a source $\delta(\mathbf{r} - \mathbf{r}_0) \delta(\mathbf{s} - \mathbf{s}_0) \delta(t)$, where $\langle \rangle$ means an ensemble average in photon direction space. Equation (1) is evaluated in Fourier space with the use of the well-known cumulant expansion theorem [16]. An algebraic closed form of expression is obtained for an arbitrary n th order cumulant. This expansion is inherently different from the spherical harmonics expansion of the photon distribution. The first-order cumulant calculation determines the *exact* center position of the photon distribution; the second-order cumulant calculation determines the *exact* half width of the photon distribution in addition; higher-order cumulant calculations provide progressively more details of the shape of the photon distribution but do not modify the cumulants of lower order. This is a major advantage of the cumulant expansion. The photon distribution approaches a Gaussian distribution as the number of scattering events increases according to the central limit theorem [16]. So it is not surprising that the second-order cumulant solution with a correct center position and

*Electronic address: minxu@sci.ccny.cuny.edu

half-width has already provided a clear picture of the time evolution of photon migration from the initial ballistic to the final diffusive regime—that photons migrate with a center that advances in time, and with an ellipsoidal contour that grows and changes shape [14].

The cumulant solution depends explicitly on the phase function of the medium and involves a complicated numerical integration over angular parameters to build a forward model. It is inconvenient for direct use in image reconstruction. An approximate form of the second-order cumulant solution relating the scattered wave field directly to the weak inhomogeneities in an infinite space was later proposed by the authors [17], which retains the main features of photon propagation at both early and later times and reduces to the conventional diffusion approximation at later times.

In this paper, we will first extend the second-order cumulant solution to planar geometries (semi-infinite and slab media) after a brief recount of the main results of the cumulant solution to the Boltzmann equation in an infinite space. The result of Monte Carlo simulations is then presented for both infinite and semi-infinite media to verify the behavior of the second-order cumulant solution at both early and later times. The weight function for image reconstruction of weak inhomogeneities is calculated with use of the simplified cumulant and diffusion approximations for semi-infinite and slab media. The results from the two approximations are compared. The advantage of this model over the diffusion approximation is then discussed.

II. THEORY

The Boltzmann equation for photon distribution function $I(\mathbf{r}, \mathbf{s}, t)$ at position \mathbf{r} , direction \mathbf{s} , and time t from a unit source at position \mathbf{r}_0 propagating along \mathbf{s}_0 at time $t=0$, is given by

$$\begin{aligned} \frac{\partial}{\partial t} I(\mathbf{r}, \mathbf{s}, t) + c\mathbf{s} \cdot \nabla_{\mathbf{r}} I(\mathbf{r}, \mathbf{s}, t) + c[\mu_s(\mathbf{r}) + \mu_a(\mathbf{r})]I(\mathbf{r}, \mathbf{s}, t) \\ = c\mu_s(\mathbf{r}) \int d\mathbf{s}' P(\mathbf{s}, \mathbf{s}') I(\mathbf{r}, \mathbf{s}', t) d\mathbf{s}' \\ + \delta(\mathbf{r} - \mathbf{r}_0) \delta(\mathbf{s} - \mathbf{s}_0) \delta(t), \end{aligned} \quad (2)$$

where c is the speed of light inside the medium, μ_a and μ_s denote the position-dependent absorption and scattering coefficients, and $P(\mathbf{s}, \mathbf{s}')$ is the normalized phase function of the light propagation in the medium. The known phase function is assumed to depend only on the scattering angle $\mathbf{s} \cdot \mathbf{s}'$, and is then expandable in Legendre polynomials,

$$P(\mathbf{s}, \mathbf{s}') = (4\pi)^{-1} \sum_l a_l P_l(\mathbf{s} \cdot \mathbf{s}'). \quad (3)$$

Equation (2) is nonseparable. However the evolution in direction space, $F(\mathbf{s}, t|\mathbf{s}_0) \exp(-\mu_a ct) = \int d\mathbf{r} I(\mathbf{r}, \mathbf{s}, t|\mathbf{r}_0, \mathbf{s}_0)$, obeys a separable equation with the solution [14]

$$F(\mathbf{s}, t|\mathbf{s}_0) = (4\pi)^{-1} \sum_l (2l+1) \exp(-g_l t) P_l(\mathbf{s} \cdot \mathbf{s}_0). \quad (4)$$

Here $g_l = c\mu_s[1 - a_l/(2l+1)]$, especially $g_0=0$ and $g_1 = c\mu'_s$ where μ'_s is the reduced scattering coefficient. The

formal solution to the Boltzmann equation, Eq. (1), is then evaluated by (1) expressing its first δ function of position \mathbf{r} as an integral of $\exp[i\mathbf{k} \cdot (\mathbf{r} - c\int_0^t \mathbf{s}(t') dt')]$ over \mathbf{k} in the Fourier space, (2) making a cumulant expansion of the latter, and (3) calculating the cumulants in the direction space with use of the exact Green's function $F(\mathbf{s}, t|\mathbf{s}_0)$ [15].

An arbitrary order of cumulant solution can be calculated [15] with higher-order cumulants providing progressively more details about the photon distribution. Because the photon distribution approaches a Gaussian distribution when the number of the scattering events increases regardless of the details of the scattering, a second-order cumulant solution is sufficient at later times. At early times, the photons' spread is narrow compared to the resolution of the detector, hence the detailed shape is less important than the correct position and half-width of the beam. We emphasize the center of the position and half-width obtained from the second-order cumulant solution is *exact* and will not be altered by higher order cumulant solutions.

The second-order cumulant solution of the photon density $N^{(0)}(\mathbf{r}, t|\mathbf{r}_0, \mathbf{s}_0) = \int d\mathbf{s} I^{(0)}(\mathbf{r}, \mathbf{s}, t|\mathbf{r}_0, \mathbf{s}_0)$ for an incident source propagating along the positive z axis ($\mathbf{s}_0 = \hat{z}$) in a uniform medium, is given by [14]

$$\begin{aligned} N^{(0)}(\mathbf{r}, t|\mathbf{r}_0, \mathbf{s}_0) = \frac{1}{(4\pi D_{zz} ct)^{1/2}} \frac{1}{4\pi D_{xx} ct} \\ \times \exp\left\{-\frac{(z-z_0-R_z)^2}{4D_{zz} ct}\right\} \\ \times \exp\left\{-\frac{(x-x_0)^2 + (y-y_0)^2}{4D_{xx} ct}\right\} \\ \times \exp(-\mu_a ct) \end{aligned} \quad (5)$$

with a moving center located at

$$R_z = l_t [1 - \exp(-ct/l_t)] \quad (6)$$

and the diffusion coefficients

$$\begin{aligned} D_{xx} = D_{yy} \\ = \frac{c}{3t} \left\{ \frac{t}{g_1} + \frac{g_2[1 - \exp(-g_1 t)]}{g_1^2(g_1 - g_2)} - \frac{1 - \exp(-g_2 t)}{g_2(g_1 - g_2)} \right\}, \\ D_{zz} = \frac{c}{3t} \left\{ \frac{t}{g_1} - \frac{(3g_1 - g_2)[1 - \exp(-g_1 t)]}{g_1^2(g_1 - g_2)} \right. \\ \left. + \frac{2[1 - \exp(-g_2 t)]}{g_2(g_1 - g_2)} - \frac{3[1 - \exp(-g_1 t)]^2}{2g_1^2} \right\}. \end{aligned} \quad (7)$$

For simplicity, we use the following approximation to the second-order cumulant solution as the background photon distribution, $I^{(0)}(\mathbf{r}, \mathbf{s}, t)$, in an infinite uniform medium [17],

$$\begin{aligned} I^{(0)}(\mathbf{r}, \mathbf{s}, t|\mathbf{r}_0, \mathbf{s}_0) = N^{(0)}(\mathbf{r}, t|\mathbf{r}_0, \mathbf{s}_0) F(\mathbf{s}, t|\mathbf{s}_0) \\ - \frac{3}{4\pi} D(t) \mathbf{s} \cdot \nabla_{\mathbf{r}} N^{(0)}(\mathbf{r}, t|\mathbf{r}_0, \mathbf{s}_0) \end{aligned} \quad (8)$$

in building the photon transport model for image reconstruction.

tion where the time-dependent diffusion coefficient $D(t)$ is taken to be an average $D(t) = (D_{xx} + D_{yy} + D_{zz})/3$ of the diffusion coefficient ellipsoid. At early times $t \rightarrow 0$, the first term of Eq. (8) dominates, and $F(\mathbf{s}, t | \mathbf{s}_0) \rightarrow \delta(\mathbf{s} - \mathbf{s}_0)$, $D(t) \rightarrow c^2 t^2 \mu_s' / 9 \rightarrow 0$, $N^{(0)}(\mathbf{r}, t | \mathbf{r}_0, \mathbf{s}_0) \rightarrow \delta(\mathbf{r} - \mathbf{r}_0 - c(t - t_0)\mathbf{s}_0)$, thus $I^{(0)}(\mathbf{r}, \mathbf{s}, t | \mathbf{r}_0, \mathbf{s}_0)$ provides a correct picture of ballistic motion of photons with speed c along the incident direction

\mathbf{s}_0 . At later times, $F(\mathbf{s}, t | \mathbf{s}_0) \rightarrow (4\pi)^{-1}$, $D(t) \rightarrow (3\mu_s')^{-1}$, Eq. (8) reduces to the photon distribution of the center-moved diffusion approximation [8].

For weak inhomogeneities, $\delta\mu_a(\mathbf{r})$ and $\delta\mu_s'(\mathbf{r})$, embedded in an otherwise uniform medium, a first-order Born approximation to Eq. (2) yields the change in the photon distribution [17]

$$\begin{aligned} \delta I(\mathbf{r}, \mathbf{s}, t | \mathbf{r}_0, \mathbf{s}_0) = & -\frac{1}{4\pi} \int dt' \int d\mathbf{r}' c \delta\mu_a(\mathbf{r}') N^{(0)}(\mathbf{r}', t - t' | \mathbf{r}, -\mathbf{s}) N^{(0)}(\mathbf{r}', t' | \mathbf{r}_0, \mathbf{s}_0) + \frac{3c}{4\pi} \int dt' \int d\mathbf{r}' D(t - t') D(t') \\ & \times [\delta\mu_a(\mathbf{r}') + \delta\mu_s'(\mathbf{r}')] \cdot \nabla_{\mathbf{r}'} N^{(0)}(\mathbf{r}', t - t' | \mathbf{r}, -\mathbf{s}) \cdot \nabla_{\mathbf{r}'} N^{(0)}(\mathbf{r}', t' | \mathbf{r}_0, \mathbf{s}_0) + \frac{3c}{4\pi} \int dt' \int d\mathbf{r}' D(t - t') \\ & \times [\delta\mu_a(\mathbf{r}') + \delta\mu_s'(\mathbf{r}')] \exp(-c\mu_s' t') \{ N^{(0)}(\mathbf{r}', t' | \mathbf{r}, -\mathbf{s}) \mathbf{s} \cdot \nabla_{\mathbf{r}'} N^{(0)}(\mathbf{r}', t - t' | \mathbf{r}_0, \mathbf{s}_0) \\ & - \mathbf{s}_0 \cdot \nabla_{\mathbf{r}'} N^{(0)}(\mathbf{r}', t - t' | \mathbf{r}, -\mathbf{s}) N^{(0)}(\mathbf{r}', t' | \mathbf{r}_0, \mathbf{s}_0) \} \end{aligned} \quad (9)$$

after neglecting fast decaying terms involving $\exp(-2g_i t)$ for $l \geq 1$. We should point out that the optical reciprocity relation is satisfied by both the photon density Eq. (5) and the photon distribution Eqs. (8) and (9). At later times, the term in Eq. (9) containing the exponential decay factor $\exp(-c\mu_s' t')$ can be neglected, the change in photon density, $4\pi \delta I(\mathbf{r}, \mathbf{s}, t)$, in the diffusive limit, is reduced to that in the diffusion approximation (Eq. (14) in Ref. [18]).

The restriction of $D(t)$ by taking an average of D_{xx} , D_{yy} , and D_{zz} can be relaxed. The diffusion coefficients $D_{xx} = D_{yy}$ and D_{zz} can be used instead. The only change is to replace all the occurrences of the form of $D(t) \nabla_{\mathbf{r}'} N^{(0)}(\mathbf{r}, t | \mathbf{r}_0, \mathbf{s}_0)$ to

$$\begin{aligned} D_{xx}(t) (\hat{x} \partial / \partial x + \hat{y} \partial / \partial y) N^{(0)}(\mathbf{r}, t | \mathbf{r}_0, \mathbf{s}_0) \\ + D_{zz}(t) \hat{z} \partial / \partial z' N^{(0)}(\mathbf{r}, t | \mathbf{r}_0, \mathbf{s}_0) \end{aligned}$$

in both Eqs. (8) and (9).

A. Extension to planar geometries

When the scattering medium is bounded, special conditions are needed to set the photon density at the interfaces. The reflection at the interface reinjects the light into the medium. Using a partial current technique, Zhu *et al.* [19] showed that the boundary condition for a semi-infinite medium can be written as

$$\left[N^{(0)} - z_e \frac{\partial N^{(0)}}{\partial z} \right]_{z=0} = 0 \quad (10)$$

at the interface $z=0$ where

$$z_e = \frac{2l_t}{3} \frac{1 - R_{\text{eff}}}{1 + R_{\text{eff}}} \quad (11)$$

Here R_{eff} is the effective reflectivity at the interface determined by the Fresnel reflection coefficients. The extrapolation length z_e measures the distance outside the medium where the energy density from the diffusion approximation vanishes linearly. A recent study by Popescu *et al.* [20] has also shown the dependence of the extrapolation length on the scattering anisotropy.

The extrapolated-boundary condition has been successfully employed for planar geometries such as a slab or a semi-infinite medium in diffuse imaging, in which the photon density is set equal to zero at an extrapolated boundary located a distance z_e outside the turbid medium [8,21,22]. The method of images is used to obtain the Green's function in such bounded media. The same technique can be applied here to the Green's function $N^{(0)}(\mathbf{r}, t | \mathbf{r}_0, \mathbf{s}_0)$.

Keeping in mind that the source approaches gradually and stops finally at $\mathbf{r}_0 + \mathbf{s}_0 l_t$ on average with the increase of time, the image of the incident point source at $(x_0, y_0, z_0 \geq 0)$ propagating along the positive z axis inside a semi-infinite medium with its interface at $z=0$ is a negative one at $(x_0, y_0, -z_0 - 2z_e - 2l_t)$ propagating along the same direction (Fig. 1). At early times, both the source and its image have not arrived at the extrapolated boundary and their contributions at the extrapolated boundary can be neglected. When the time increases, the contributions at the extrapolated boundary from both the source and image tend to cancel each other as both approach their final stops (shadow spots in Fig. 1). The shadow spots just represent the positions of the source and its image in the center-moved diffusion approximation. The Green's function of a semi-infinite medium given by

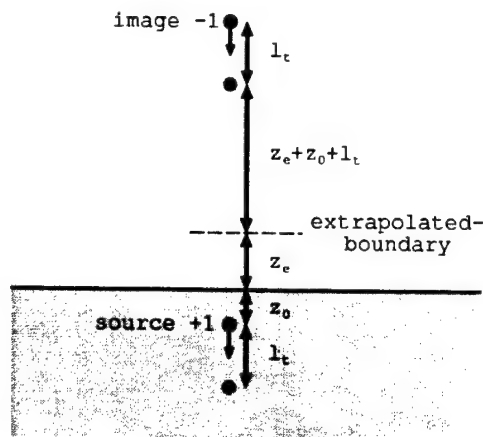


FIG. 1. The incident source at position $(x_0, y_0, z_0 \geq 0)$ and its image source at $(x_0, y_0, -z_0 - 2z_e - 2l_t)$ propagating along the positive z axis in a semi-infinite medium ($z \geq 0$) with its interface at $z = 0$. The source and its image move from their original positions (dark spots) to their final stops (shadow spots) at later times.

$$N_{\text{semi}}^{(0)}(\mathbf{r}, t | \mathbf{r}_0, \mathbf{s}_0) = N^{(0)}(\mathbf{r}, t | x_0, y_0, z_0, \mathbf{s}_0) - N^{(0)}(\mathbf{r}, t | x_0, y_0, -z_0 - 2z_e - 2l_t, \mathbf{s}_0) \quad (12)$$

thus approximately satisfies the extrapolated-boundary condition.

The same procedure can be easily applied to a slab with its extrapolated boundaries at $z = 0$ and $z = L$. The images of an incident source at (x_0, y_0, z_0) with $0 \leq z_0 \leq L$ propagating along positive or negative z axis ($s_z = \pm 1$) are a set of positive images at $(x_0, y_0, z_0 + 2nL)$ and a set of negative ones at $(x_0, y_0, -z_0 - 2nL - 2s_z l_t)$, all propagating along the same direction as the source ($-\infty < n < \infty$ is integer).

B. Comparison with the Monte Carlo simulation

We will compare the photon densities computed by the diffusion approximation (DA), the cumulant approximation (CA) Eqs. (5) and (8), and the Monte Carlo method (MC) for an incident collimated pulse first in an infinite space and then in a semi-infinite space. In DA, the incident photons are assumed initially scattered isotropically at a depth of one transport mean free path into the medium as used by Patterson *et al.* [8]. No such adjustments are performed in CA. The Monte Carlo code is adapted from Prahl *et al.* [23] and Wang *et al.* [24]. Photons are launched one by one into the medium. Each photon (regarded as a packet) starts from the origin of the coordinate system and the first scattering event takes place along the positive z axis. The step size (distance between consecutive scattering events) is sampled from an exponential distribution characterized by the total attenuation $\mu_T = \mu_s + \mu_a$, following Beer's law. After each propagation step, the photon packet is split into two parts—a fraction (μ_a / μ_T) is absorbed and the rest scattered. The new propagation direction after scattering (three directional cosines) is sampled by assuming a Henyey-Greenstein phase function [25]. The effect of internal reflection is included in this code. The technique of roulette [26] is used to terminate a photon

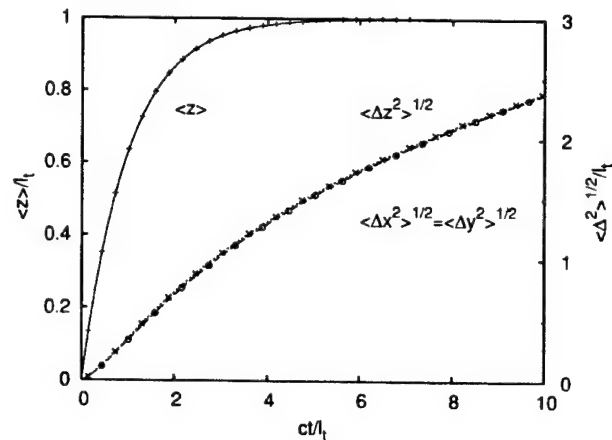


FIG. 2. The center position and the half-width of the photon cloud inside a uniform infinite absorptionless medium with anisotropy equal to 0.9.

packet to improve the efficiency of the calculation without introducing a bias. The results in the following paragraphs have been scaled to use the transport mean free path l_t as the unit of the length and the flight time for one transport mean free path in the medium l_t/c as the unit of the time. The source is incident along the positive z axis at the origin in space and time. 5×10^6 photons are used in one run of the Monte Carlo simulation.

The first- and second-order cumulants (the center position and the half-width of the “photon cloud”) of our cumulant solution Eq. (5) is

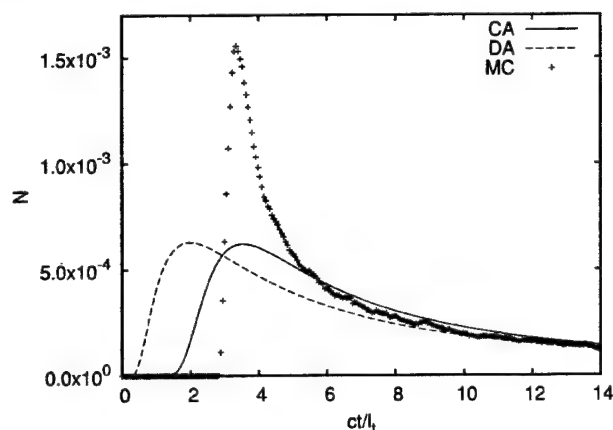
$$\langle x(t) \rangle = \langle y(t) \rangle = 0, \quad \langle z(t) \rangle = l_t [1 - \exp(-ct/l_t)],$$

$$\sqrt{\langle \Delta x(t)^2 \rangle} = \sqrt{\langle \Delta y(t)^2 \rangle} = \sqrt{2D_{xx}(t)ct},$$

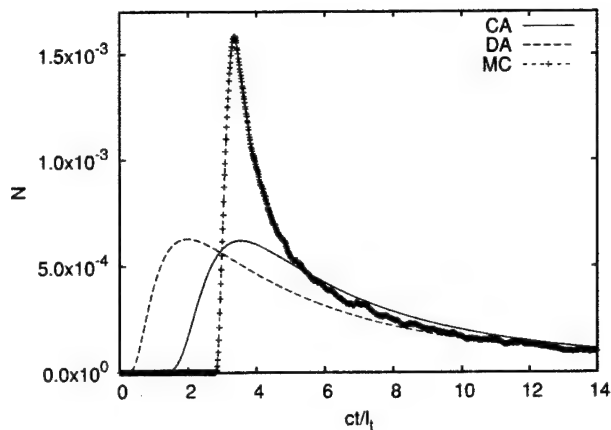
$$\sqrt{\langle \Delta z(t)^2 \rangle} = \sqrt{2D_{zz}(t)ct}, \quad (13)$$

where $\langle \rangle$ means an ensemble average of photon positions at a specified time. This theoretical prediction can be easily verified by a Monte Carlo simulation. Figure (2) shows the first two cumulants of photons for an incident pulse along the z axis at time zero into an infinite medium with anisotropy 0.9. A perfect agreement on the center position (the first-order cumulant) and the half-width (the second order cumulant) of the photon distribution between our theoretical result and the Monte Carlo simulation is obtained. The half-widths along xyz directions are very close; the value along z direction is a bit larger than that along the xy direction as predicted by Eq. (13).

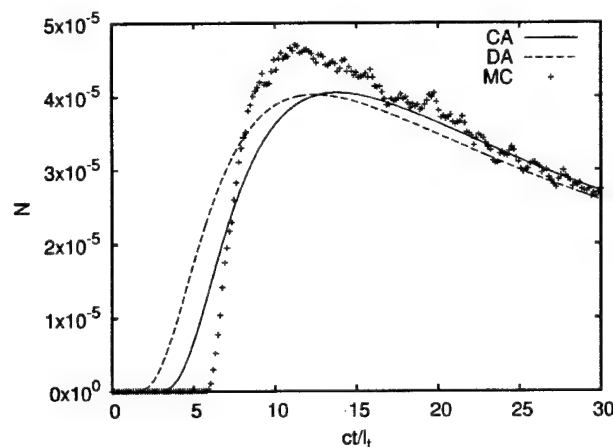
Figures 3(a)–3(c) shows the photon density at positions $(0, 0, 3l_t)$, $(0, 0, 6l_t)$, and $(0, 0, 10l_t)$ computed by all three different methods for the same infinite medium. At a distance of $3l_t$, the time profile of photon density from the cumulant approximation agrees much better to the Monte Carlo result than DA by providing a correct peak position of photon density. Some amount of photons arriving faster than the speed of light still exist in this second-order cumulant calculation. However, this is already a big improvement compared to DA. The result from CA can be further improved when higher-order cumulants are used. At a larger distance, all the



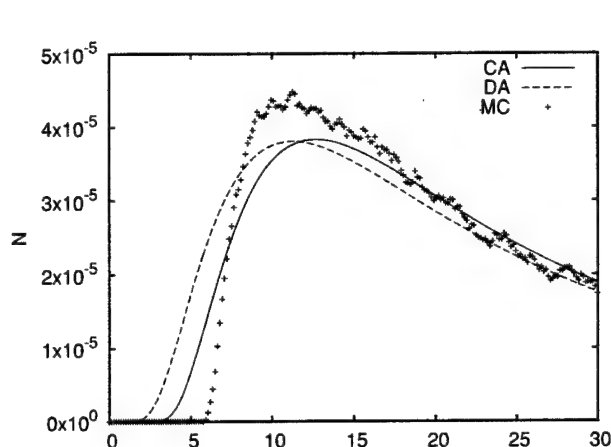
(a)



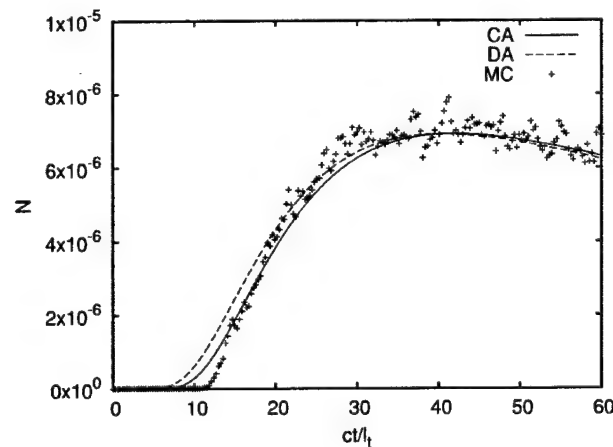
(a)



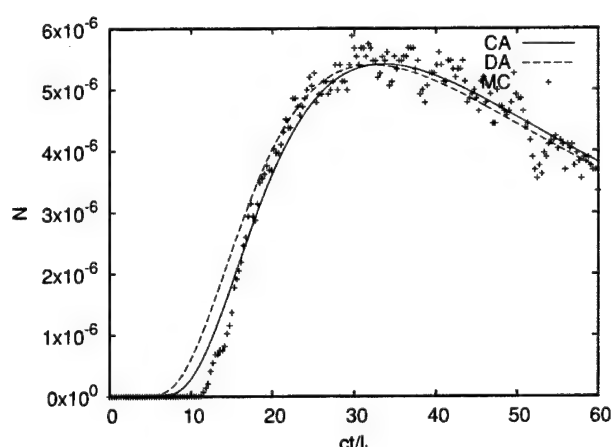
(b)



(b)



(c)



(c)

FIG. 3. Photon density at positions (a) $(0,0,3l_t)$, (b) $(0,0,6l_t)$, and (c) $(0,0,10l_t)$ vs time normalized to a unit source in an infinite medium. The source is incident along the positive z axis at the origin of the coordinate system and at time zero. The three curves are computed by the diffusion approximation (DA), the cumulant approximation (CA), and the Monte Carlo method (MC), respectively.

FIG. 4. Photon density at positions (a) $(0,0,3l_t)$, (b) $(0,0,6l_t)$, and (c) $(0,0,10l_t)$ vs time normalized to a unit source in a semi-infinite medium. The source is incident normal to the surface of the medium and along the positive z axis at the origin of the coordinate system and at time zero.

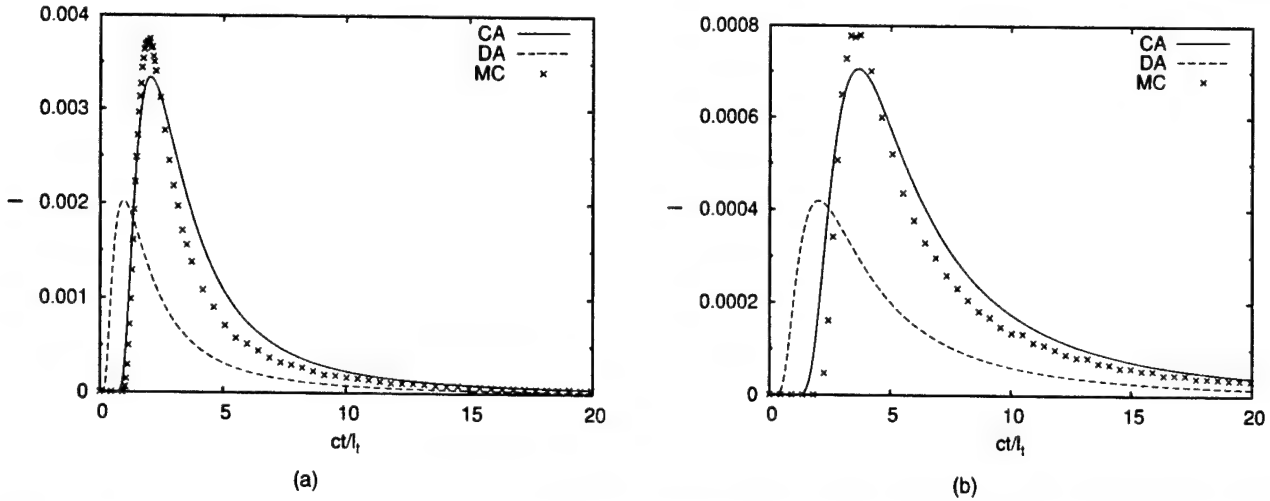


FIG. 5. The backscattered photon intensity $I(\mathbf{r}, -\hat{\mathbf{z}}, t)$ at positions (a) $(0, l_i, 0)$ and (b) $(0, 2l_i, 0)$ on the boundary of a semi-infinite medium vs time normalized to a unit source in a semi-infinite medium. The source is incident normal to the surface of the medium and along the positive z axis at the origin of the coordinate system and at time zero.

three methods begin to agree with each other pretty well and the cumulant approximation is better than the diffusion approximation. The difference between results from DA, CA, and MC is negligible when the distance is $10l_i$ or larger.

The calculations using DA, CA, and MC are performed again for a semi-infinite medium with its boundary at $z=0$, whose optical parameters are taken to be the same as the above infinite medium. The source is incident at the origin of the coordinate system and along the positive z axis (normal to the surface) at time zero. The effective reflectivity is taken to be zero and an extrapolation length $z_e = 0.7l_i$ is used in both DA and CA calculations. Figures 4(a)–4(c) shows the corresponding results for this example. Again CA shows a much better agreement to the MC than DA. Compared with Fig. 3 for the infinite case, the tail of the profiles in Figs. 4(a)–4(c) for the semi-infinite medium is lower due to the presence of an extra negative image source coming from the boundary condition.

As a final example, the backscattered photon intensity $I^{(0)}(\mathbf{r}, -\hat{\mathbf{z}}, t)$ at positions $(0, l_i, 0)$ and $(0, 2l_i, 0)$ on the boundary of the above semi-infinite medium is calculated with use of the three different methods (see Fig. 5). In DA, photons diffuse from the adjusted source position $(0, 0, l_i)$ with the constant diffusion coefficient $D = l_i/3$. In CA, back-scattered photons arrive later because the center of photons moves

forward along the positive z direction and diffuse from the moving center with a gradually increasing diffusion coefficient from 0 to $l_i/3$. CA agrees well with the Monte Carlo simulation.

C. Weight function for image reconstruction

The response (the change of the scattered wave field) to a unit absorption or scattering inhomogeneity is usually called the weight function or the Jacobian in medical tomography literature. This quantity plays a central role in image reconstruction regardless of which method is used to obtain the inhomogeneity distribution in a medium. Let us rewrite Eq. (9) in the following form:

$$4\pi\delta I(\mathbf{r}, \mathbf{s}, t | z_0, \mathbf{s}_0) = -c \int d\mathbf{r}' \delta\mu_a(\mathbf{r}') w_a(\mathbf{r}, \mathbf{s}, \mathbf{r}_0, \mathbf{s}_0, t; \mathbf{r}') + \frac{c}{3\mu_s'^2} \int d\mathbf{r}' \delta\mu_s'(\mathbf{r}') \times w_s(\mathbf{r}, \mathbf{s}, \mathbf{r}_0, \mathbf{s}_0, t; \mathbf{r}') \quad (14)$$

with the absorption and scattering weight functions defined as

$$w_a(\mathbf{r}, \mathbf{s}, \mathbf{r}_0, \mathbf{s}_0, t; \mathbf{r}') = \int_0^t dt' N^{(0)}(\mathbf{r}', t-t' | \mathbf{r}, -\mathbf{s}) N^{(0)}(\mathbf{r}', t' | \mathbf{r}_0, \mathbf{s}_0) - w_s(\mathbf{r}, \mathbf{s}, \mathbf{r}_0, \mathbf{s}_0, t; \mathbf{r}') / (3\mu_s'^2) \\ \frac{w_s(\mathbf{r}, \mathbf{s}, \mathbf{r}_0, \mathbf{s}_0, t; \mathbf{r}')}{9\mu_s'^2} = \int_0^t dt' D(t-t') D(t') \nabla_{\mathbf{r}'} N^{(0)}(\mathbf{r}', t-t' | \mathbf{r}, -\mathbf{s}) \cdot \nabla_{\mathbf{r}'} N^{(0)}(\mathbf{r}', t' | \mathbf{r}_0, \mathbf{s}_0) + \int_0^t dt' D(t') \\ \times \exp[-c\mu_s'(t-t')] N^{(0)}(\mathbf{r}', t-t' | \mathbf{r}, -\mathbf{s}) \mathbf{s} \cdot \nabla_{\mathbf{r}'} N^{(0)}(\mathbf{r}', t' | \mathbf{r}_0, \mathbf{s}_0) - \int_0^t dt' D(t-t') \\ \times \exp(-c\mu_s't') \mathbf{s}_0 \cdot \nabla_{\mathbf{r}'} N^{(0)}(\mathbf{r}', t-t' | \mathbf{r}, -\mathbf{s}) N^{(0)}(\mathbf{r}', t' | \mathbf{r}_0, \mathbf{s}_0), \quad (15)$$

respectively.

As $N^{(0)}(\mathbf{r}, t | \mathbf{r}_0, \mathbf{s}_0) \rightarrow \delta(\mathbf{r} - \mathbf{r}_0 - c t \mathbf{s}_0)$ when $t \rightarrow 0$, special attentions must be paid when a numerical integration is carried out for Eq. (15). The range of integration is divided into three areas: $(0, \Delta)$, $(\Delta, t - \Delta)$, and $(t - \Delta, t)$ where $t \gg \Delta > 0$. The end corrections from the integration over $(0, \Delta)$ and $(t - \Delta, t)$ to the weight functions integrated over $(\Delta, t - \Delta)$ range are approximately given by

$$e_a(\mathbf{r}, \mathbf{s}, \mathbf{r}_0, \mathbf{s}_0, t; \mathbf{r}') = \frac{1}{c} N(\mathbf{r}', t | \mathbf{r}, -\mathbf{s}) \delta(x' - x_0) \delta(y' - y_0) H(\Delta - \xi) H(\xi) + \frac{1}{c} N(\mathbf{r}', t | \mathbf{r}_0, \mathbf{s}_0) \delta(x' - x) \delta(y' - y) H(\Delta - \eta) H(\eta) - e_s(\mathbf{r}, \mathbf{s}, \mathbf{r}_0, \mathbf{s}_0, t; \mathbf{r}') / (3\mu_s'^2),$$

$$\frac{e_s(\mathbf{r}, \mathbf{s}, \mathbf{r}_0, \mathbf{s}_0, t; \mathbf{r}')}{9\mu_s'^2} = -\frac{D(t)}{c} \left(1 - \frac{\partial D(t)}{c \partial t} \right) \bigg|_{t=\xi} \mathbf{s}_0 \cdot \nabla_{\mathbf{r}'} N(\mathbf{r}', t | \mathbf{r}, -\mathbf{s}) \delta(x' - x_0) \delta(y' - y_0) H(\Delta - \xi) H(\xi) + \frac{D(t)}{c} \times \left(1 - \frac{\partial D(t)}{c \partial t} \right) \bigg|_{t=\eta} \mathbf{s} \cdot \nabla_{\mathbf{r}'} N(\mathbf{r}', t | \mathbf{r}_0, \mathbf{s}_0) \delta(x' - x) \delta(y' - y) H(\Delta - \eta) H(\eta), \quad (16)$$

where $\mathbf{r}' = \mathbf{r}_0 + c \xi \mathbf{s}_0 = \mathbf{r} - \eta c \mathbf{s}$ is the position of the inhomogeneity, \mathbf{s} and \mathbf{s}_0 are assumed to be along the positive or negative z axis, and H is the Heaviside function. In the following calculations, the refractive index of the medium is assumed to be 1.33; the absorption and scattering coefficients of the medium are assumed to be 0.003 mm^{-1} and 10 mm^{-1} , respectively, and the scattering anisotropy 0.9, providing a transport mean free path $l_t = 1 \text{ mm}$. The offset Δ is taken to be 0.1 ps when more than 99% of the photon packet still concentrates within a cubic volume $(0.01l_t)^3$. The weight function from a cubic of volume $(0.01l_t)^3$ is calculated using the DCUHRE algorithm [27].

The weight functions for a semi-infinite medium are shown in Fig. 6 for absorption and scattering inhomogeneities. The backscattered photons (propagating along negative z axis) are detected by a detector placed at a position $(0, 2l_t, 0)$, off two transport mean free path from the source. Figures 6(a) and 6(c) show the response to an inhomogeneity at $(0, 0, z)$ positions which is in the propagation direction of the source at delay 50 ps and 500 ps. The CA shows a much stronger response from the inhomogeneity in the propagation direction of and close to the source than the diffusion approximation. Both absorption and scattering weight functions from CA reveal a peak at about $0.03l_t$. This peak originates from the initial ballistic motion of the incident photon. In a short time after the photon is launched ($t \rightarrow 0$), the photon packet will be positioned at $z^* = ct$ with a spread of half-width $\approx \sqrt{4D(t)ct} = 2ct\sqrt{ct/(3l_t)}$, hence the presence of an absorption or scattering inhomogeneity at position $(0, 0, z < z^*)$, sitting in the ballistic path of the photon, will significantly reduce the number of backscattered photons received by the detector [$w_a > 0$ and $w_s < 0$ in Eq. (14)]. In Figs. 6(b) and 6(d) where the inhomogeneity is placed at $(0, l_t, z)$ mm positions, not sitting in the ballistic path of the photon, this peak is gone.

The diffusion approximation is invalid when the inhomogeneity is too close to the source or the detector. Nevertheless, the weight function from DA is plotted over the full z

range for comparison. A peak is found in the absorption weight function [Fig. 6(a)] and a crossing of zero in the scattering weight function [Fig. 6(c)] at $z = l_t$, because of the artificial adjustment of the source position to one transport mean free path into the medium and the singularity of the Green's function in DA when the inhomogeneity and the source overlap.

A larger disagreement between CA and DA is observed in the scattering weight function than in the absorption weight function. The absorption weight functions from CA and DA agree with each other relatively well except for a region of depth of l_t near the surface when the inhomogeneity is in the propagation direction of the source, or in the field of view of the detector. The scattering weight functions from CA and DA disagree significantly within the region of depth of at least $2l_t$ close to the surface. The deepest position that can be detected by the detector at time t is roughly $ct/2$. This condition is better observed by CA because CA shows a faster decay rate of both the absorption and scattering weight functions with the increase of the depth [Figs. 6(a)–6(d)].

The absorption and scattering weight functions for a slab is shown in Fig. 7. The slab has the same optical parameter as the semi-infinite medium. The thickness of the slab is $d = 30l_t$. The source is at the origin $(0, 0, 0)$. The detector is placed on the opposite side of the slab, $(0, 0, 30l_t)$, in the propagation direction of the source. The weight functions by the cumulant approximation and the diffusion approximation are strictly symmetric about the plane $z = d/2$. The agreement between CA and DA for the absorption weight function is better than for the scattering weight function. Both CA and DA produce close results for the inhomogeneity not located near the boundary. When the inhomogeneity is placed along the line $(0, 0, z)$, in the propagation direction of the source and in the field of view of the detector, two peaks at about $0.03l_t$ and $d - 0.03l_t$ appear in CA; two peaks in the absorption weight function [Fig. 7(a)] and two crossings of zero in the scattering weight function [Fig. 7(c)] appear in DA at l_t and $d - l_t$.

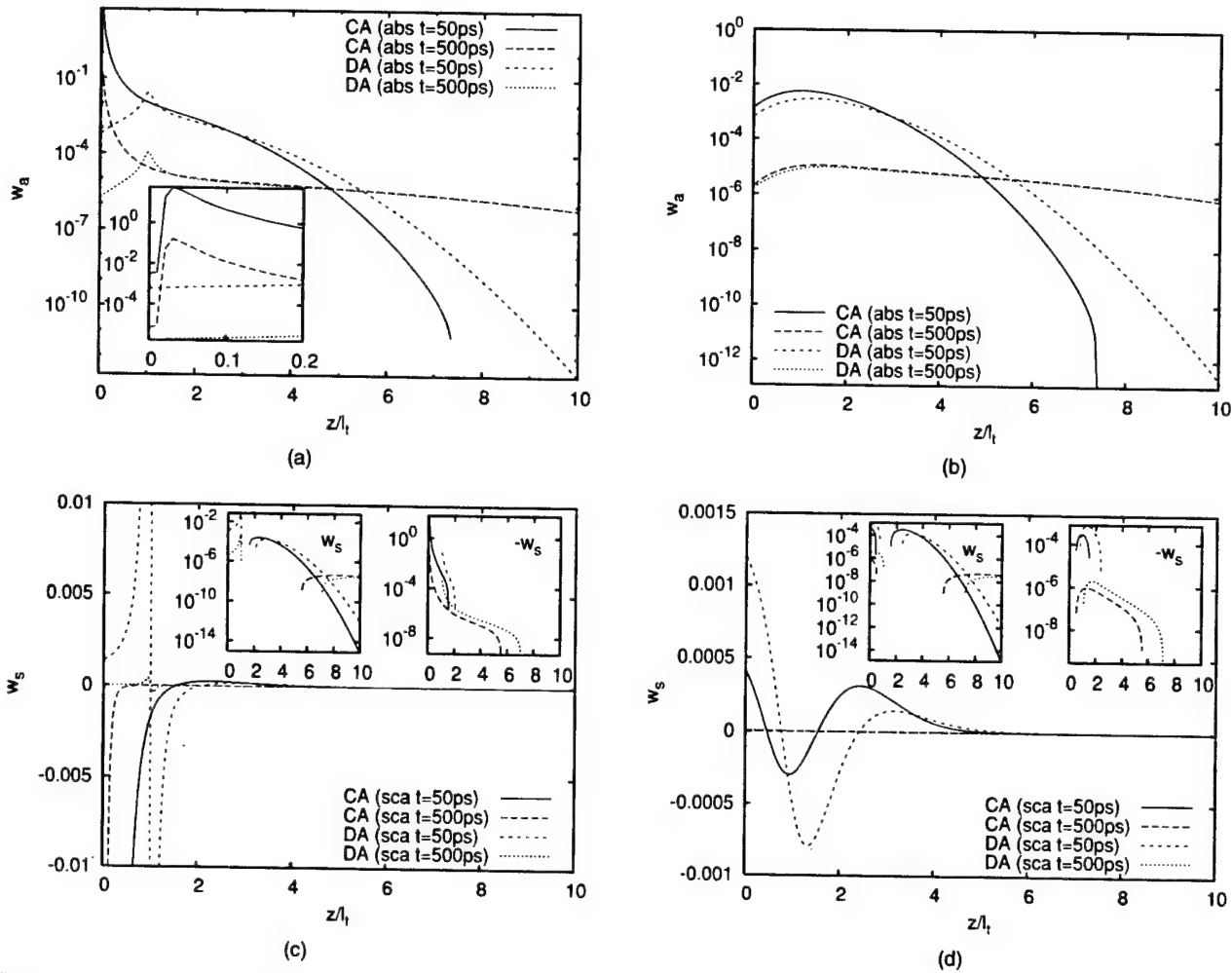


FIG. 6. Weight functions for a semi-infinite medium where the inhomogeneity is (a) absorption and (c) scattering at $(0,0,z)$, in the propagation direction of the source; (b) absorption and (d) scattering at $(0,l_i,z)$, off by one transport mean free path. Profiles at two delay times $t=50$ ps and $t=500$ ps are plotted for both the cumulant approximation (CA) and the diffusion approximation (DA). The insets replot the weight functions in a logarithm scale.

III. DISCUSSION

We attribute the formation of a peak very close to the surface but not on the surface (about $0.03l_i$ into the medium) of the absorption and scattering weight function in the cumulant approximation to the initial ballistic motion of the incident photon. The photon penetrates into the medium with an initial speed of c and with its center approaching and stopping at one transport mean free path into the medium. Hence the effect is only significant when the inhomogeneity is in the propagation direction of the source or in the field of view of the detector, and the peak response shifts away from the surface of the medium.

The diffusion approximation requires one to adjust the position of the source to compensate for the initial ballistic motion of the photon [8,28,29]. From our more accurate result Eq. (9), the source and the detector terms appear in a form of $N^{(0)}(\mathbf{r}', \tau | \mathbf{r}, -\mathbf{s})$ and $N^{(0)}(\mathbf{r}', \tau | \mathbf{r}_0, \mathbf{s}_0)$, respectively. The source and the detector approach gradually and stop at $\mathbf{r}_0 + l_i \mathbf{s}_0$ and $\mathbf{r} - l_i \mathbf{s}$, respectively, with the increase of time

where \mathbf{s}_0 and \mathbf{s} are the propagating directions of the incident and outgoing photon. The positioning of both the source and the detector for one transport mean free path into the medium is hence mandatory if the diffusion approximation is used. The curves for DA in Figs. 6 and 7 are calculated using this adjustment. The DA will deviate from the CA significantly over the full range of depth if the adjustment on the position of the source or the detector is not performed.

The diffusion approximation for image reconstruction substantially underestimates the contribution to the emission measurement from the inhomogeneity in the propagation direction of and close to the source, or in the field of view and close to the detector. This error may distort the signal from the inhomogeneity inside the medium because the weight function near surface is usually much larger than that inside, and may lead to a failure in image reconstruction. The high response from the region near surface is not desirable when the inhomogeneity inside the medium is to be detected in the transmission or backscattering measurements. The cancella-

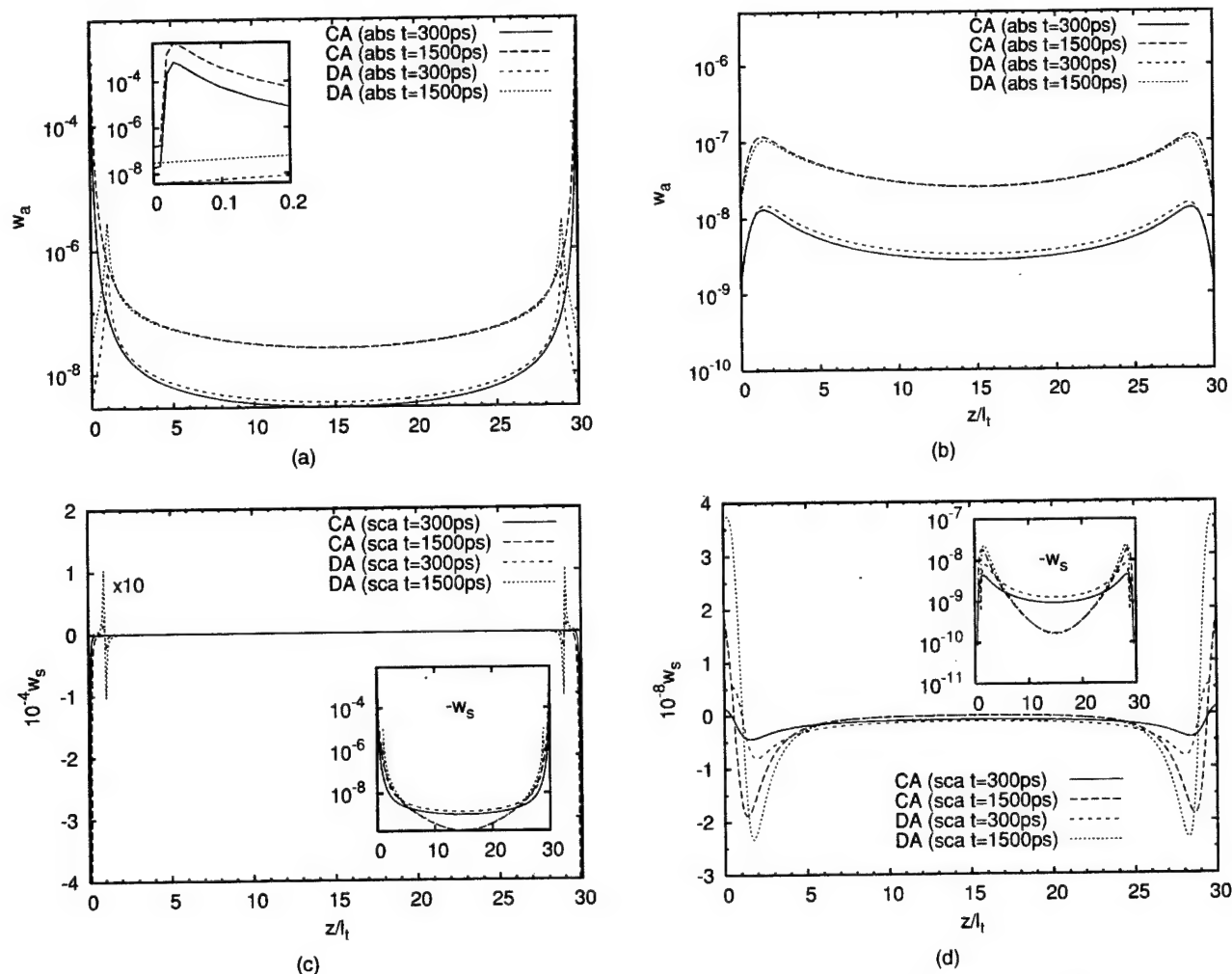


FIG. 7. Weight function for a slab where the inhomogeneity is (a) absorption and (c) scattering at $(0,0,z)$, in the propagation direction of the source, (b) absorption and (d) scattering at $(0,l_t,z)$, off by one transport mean free path. Weight functions calculated from the cumulant (CA) and diffusion (DA) approximations are plotted for time delays of $t = 300$ ps and $t = 1500$ ps. The insets replot the weight functions in a logarithm scale.

tion between multiple measurements using nearby wavelengths may help reduce this effect.

Other attempts to obtain a better approximation to radiative transfer in turbid media were made by various authors such as Ishimaru's diffusion approximation [30,31], the telegrapher equation of Durian *et al.* based on the two stream theory [32], Gershenson's time-dependent equation in the diffusion limit using a higher-order angular expansion [6], and non-Euclidean diffusion equation of Polishchuk *et al.* [33]. The advantage of this cumulant approximation is that it provides a clear picture of photon migration for an incident collimated beam from early to later times and that it gives the *exact* center and the *exact* spread of the photon cloud at both early and later times by only using a second-order cumulant approximation.

In conclusion, we have presented a cumulant approximation to radiative transfer, which provides an analytical tool to describe photon migration at both early and later times—

from the initial ballistic motion till the final diffuse regime. To a second-order cumulant, the solution agrees with the Monte Carlo simulation at later times and provides a correct peak position in time for photon arrivals at early times, in both an infinite medium and a bounded medium with a planar geometry. The initial ballistic motion of photon produces a strong peak in the response from absorption and/or scattering inhomogeneities, which are in the propagation direction of and close to the source, or in the field of view of and close to the detector, at both early and later times.

ACKNOWLEDGMENTS

This work was supported in part by the U.S. Army Medical Research Material Command, NASA Institutional Research Award, the New York State Office of Science, Technology and Research, and the U.S. Department of Energy.

- [1] S. Chandrasekhar, *Radiation Transfer* (Oxford University Press, Oxford, 1950).
- [2] J. J. Duderstadt and W. R. Martin, *Transport Theory* (Wiley, New York, 1979).
- [3] A. Ishimaru, *Wave Propagation and Scattering in Random Media* (Academic, New York, 1978), Vols. I and II.
- [4] C. Cercignani, *The Boltzmann Equation and its Applications*, Applied Mathematical Sciences Vol. 67 (Springer-Verlag, Berlin, 1988).
- [5] G. D. Mahan, *J. Math. Phys.* **36**, 6758 (1995).
- [6] M. Gershenson, *Phys. Rev. E* **59**, 7178 (1999).
- [7] K. M. Yoo, F. Lin, and R. R. Alfano, *Phys. Rev. Lett.* **64**, 2647 (1990).
- [8] M. S. Patterson, B. Chance, and B. C. Wilson, *Appl. Opt.* **28**, 2331 (1989).
- [9] S. Fantini *et al.*, *Proc. SPIE* **2389**, 204 (1995).
- [10] *J. Opt. Soc. Am. A* **14**, 136 (1997), special issue on diffusing photons in turbid media, edited by A. G. Yodh, B. Tromberg, E. Sevick-Muraca, and D. Pine.
- [11] J. C. Hebden, S. R. Arridge, and D. T. Delpy, *Phys. Med. Biol.* **42**, 825 (1997).
- [12] S. R. Arridge and J. C. Hebden, *Phys. Med. Biol.* **42**, 841 (1997).
- [13] *Proceedings of Inter-Institute Workshop on In Vivo Optical Imaging at the NIH*, edited by A. H. Gandjbakhche (Optical Society of America, Washington, D.C. 1999).
- [14] W. Cai, M. Lax, and R. R. Alfano, *Phys. Rev. E* **61**, 3871 (2000).
- [15] W. Cai, M. Lax, and R. R. Alfano, *J. Phys. Chem. B* **104**, 3996 (2000).
- [16] S. H. Ma, *Statistical Mechanics* (World Scientific, Philadelphia, 1985).
- [17] M. Wu, W. Cai, M. Lax, and R. R. Alfano, *Opt. Lett.* **26**, 1066 (2001).
- [18] S. R. Arridge, *Appl. Opt.* **34**, 7395 (1995).
- [19] J. X. Zhu, D. J. Pine, and D. A. Weitz, *Phys. Rev. A* **44**, 3948 (1991).
- [20] G. Popescu, C. Mujat, and A. Dogariu, *Phys. Rev. E* **61**, 4523 (2000).
- [21] R. C. Haskell, I. O. Svaasand, T.-T. Tsay, T.-C. Feng, M. S. McAdams, and B. J. Tromber, *J. Opt. Soc. Am. A* **11**, 2727 (1994).
- [22] J. C. J. Paasschens and G. W. 't Hooft, *J. Opt. Soc. Am. A* **15**, 1797 (1998).
- [23] S. A. Prahl, M. Keijzer, S. L. Jacques, and A. J. Welch, *Proc. SPIE* **IS-5**, 102 (1989).
- [24] L. H. Wang, S. L. Jacques, and L. Q. Zheng, *Comput. Methods Programs Biomed.* **47**, 131 (1995).
- [25] L. G. Henyey and J. L. Greenstein, *Astrophys. J.* **93**, 70 (1941).
- [26] R. Y. Rubinstein, *Simulation and the Monte Carlo Method* (Wiley, New York, 1981).
- [27] J. Berntsen, T. O. Espelid, and A. Genz, *ACM Trans. Math. Softw.* **17**, 452 (1991).
- [28] J. S. Maier and E. Gratton, *Proc. SPIE* **1888**, 440 (1993).
- [29] Y. Tsuchiya, K. Ohta, and T. Urakami, *Jpn. J. Appl. Phys., Part 1* **34**, 2495 (1995).
- [30] A. Ishimaru, *J. Opt. Soc. Am.* **68**, 1045 (1978).
- [31] A. Ishimaru, *J. Opt. Soc. Am. A* **1**, 506 (1984).
- [32] D. J. Durian and J. Rudnick, *J. Opt. Soc. Am. A* **14**, 940 (1997).
- [33] A. Y. Polishchuk and R. R. Alfano, *Opt. Lett.* **21**, 916 (1996).

Cancerous and normal human tissues investigated by near-infrared time-resolved and spectroscopic imaging techniques

M. Alrubaiee^a, S. K. Gayen^a, J. A. Koutcher^b, and R. R. Alfano^a

^aInstitute for Ultrafast Spectroscopy and Lasers, and Physics Department

The City College of New York, 138th Street at Convent Avenue, New York, NY 10031

^bMemorial Sloan Kettering Cancer Center, 1275 York Avenue, New York, NY 10021

ABSTRACT

Spectroscopic and time-sliced two-dimensional (2-D) transillumination imaging methods were used to investigate *ex vivo* tumor and normal tissues of human breast and parotid gland. The experimental arrangement for time-sliced optical imaging uses 120-fs, 1 kHz repetition-rate, 800-nm light pulses from a Ti:sapphire laser system for sample illumination and a charge coupled device (CCD) camera coupled to a gated image intensifier for recording 2-D images. The spectroscopic imaging arrangement uses 1210-1325 nm tunable output of a Cr: forsterite laser for sample illumination, a Fourier space gate to discriminate against multiple-scattered light, and a near-infrared (NIR) area camera to record 2-D images. Images recorded with earlier temporal slices of transmitted light highlighted tumors, while those recorded with later slices accentuated normal tissues. When light was tuned closer to the 1203 nm absorption resonance of adipose tissues, a marked enhancement in contrast between the images of adipose and fibrous tissues was observed. A similar wavelength-dependent difference between normal and cancerous tissues was observed. These results correlate well with pathology and nuclear magnetic resonance based analyses of the samples. This work demonstrates the advantages of time-resolved spectroscopic approach for imaging tumors in body organs.

Keywords: Time-resolved optical imaging, near-infrared spectroscopic imaging, breast cancer, nuclear magnetic resonance, noninvasive cancer detection, parotid gland, Warthin's tumor

1. INTRODUCTION

The need for noninvasive imaging modalities for early detection and diagnosis of cancer drives the recent research interest in developing NIR light based imaging techniques.¹⁻⁴ Many researchers use measurement of amplitude and phase of photon density wave launched in a tissue specimen upon irradiation with frequency-modulated NIR light to obtain images of the target specimen.⁴ We have developed a fast, time-resolved imaging approach⁵⁻⁷ because it is intuitive simple and can provide simultaneous information at a multitude of frequencies that is useful for three-dimensional image reconstruction. We complement the time-sliced imaging at 800 nm with continuous wave (CW) spectroscopic imaging that uses NIR light in the therapeutic wavelength range of 1200-1350 nm to realize the diagnostic potential of optical imaging approach.⁸

An important step in the development of a noninvasive optical imaging approach is testing its efficiency on *ex-vivo* tissue specimens of the target organ, which in turn provides key information about light transport and optical characteristics of the types of tissues under investigation. In this article we present result of measurements on human breast and parotid gland tissues.

2. EXPERIMENTAL ARRANGEMENT

Our experimental arrangement for time-sliced imaging, detailed elsewhere,⁵⁻⁷ made use of approximately 120-fs duration, 1-kHz repetition-rate, 800-nm light pulses from a Ti-sapphire laser and amplifier system⁹ for sample illumination, and an ultrafast gated intensified camera system (UGICS) for recording 2-D images.⁷ The UGICS system provides a 80-ps time gate whose position can be varied over a 20 ns range.⁷ The arrangement for NIR spectroscopic imaging used the output of a Cr⁴⁺: forsterite laser to illuminate the sample. A Fourier space gate¹⁰ selected out a fraction of the less scattered image-bearing photons, and a 50 mm focal-length camera lens directed them to the 320 x 240 pixels imaging element of an InGaAs NIR area camera. A 10 mm x 20 mm x 5 mm thick human breast tissue specimen

composed of normal adipose (NA), and cancerous (C) tissues was used in the experiment. The sample obtained from the left breast of a 63-year old female following a modified radical mastectomy and lymph node dissection at the Memorial Sloan-Kettering Cancer Center (MSKCC) was provided to us under an Institutional Review Board (IRB) approval from CCNY. The clinical diagnosis revealed an invasive ductal carcinoma (IDC) with poorly differentiated histologic grade III/III and nuclear grade III/III. The specimen was placed in a high grade Pyrex glass (suitable for both optical and NMR studies) container that slightly compressed and retained the tissue axial orientation. Following the optical imaging, the undisturbed sample cell was transferred to MSKCC and weighted T_1 and T_2 relaxation time NMR images of the sample were recorded.^{11,12}

The 20 mm x 20 mm x 10 mm excised parotid gland tissue specimen was obtained from the New York Eye and Ear Infirmary (NYEEI), under an IRB approval from CCNY. The sample was placed between two glass slides and mildly compressed to maintain a uniform thickness. The specimen came from the left parotid gland of a 37-year-old male patient. The clinical diagnosis revealed a Warthin's tumor¹³ (WT) of the left parotid gland (PG).

3. EXPERIMENTAL RESULTS

3.1 Time-sliced imaging

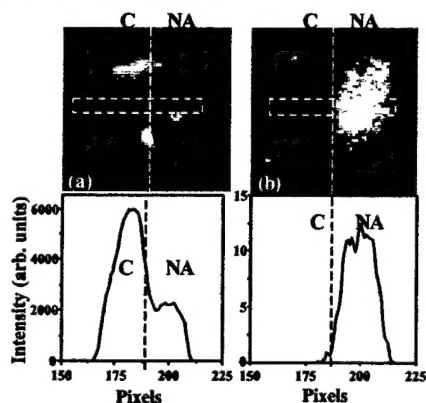


Fig. 1 Time-sliced images of the breast tissue specimen at the gate position of (a) 25 ps, and (b) 225 ps.

intensity profiles exhibit peak in the cancer (C) region. At this early time, markedly more light is transmitted through the tumor than through the normal tissue. With time the normal tissue image gain in brightness as shown in the 225-ps image of Fig. 1(b). The corresponding spatial intensity profile peaks in the normal (N) position indicating higher light transmission through the normal region than the tumor. This result indicates that light transmits faster through tumor than normal tissue. Lower scattering or/and higher absorption of light by the tumor may account for the observed temporal behavior. Since, there is no known absorption of 800-nm light by the breast tissue, we attribute these time-dependent differences in transmitted light intensity to higher scattering of light by normal tissue than the cancerous tissue.

Similar time-dependent differences in transmitted light intensity and image characteristics are observed between the Warthin's tumor and the normal regions of the parotid gland tissue sample, as shown in Figs. 2(a) and 2(b).

3.2 Spectroscopic imaging

Spectroscopic images of the breast tissue sample recorded using light of wavelength 1225 nm, and 1300 nm appear in the upper frames of Figs. 3(a) and 3(b), respectively. Corresponding spatial profiles integrated over the same horizontal

Time-sliced 2-D transillumination images of the breast tissue sample for gate positions of 25-ps and 225-ps are displayed in the upper frames of Figs. 1(a) and 1(b), respectively. The zero position was taken to be the time of arrival of a light pulse through a 5-mm thick quartz cell filled with water. The corresponding lower frames present the spatial intensity profiles of the respective images integrated over the same horizontal area in both the images. The salient feature of the images is the difference in time-dependent brightness of the normal tissue (N) and cancer (C) regions in the sample. In the 25-ps image of Fig. 1(a) the cancer region (C) is prominent. The corresponding horizontal spatial

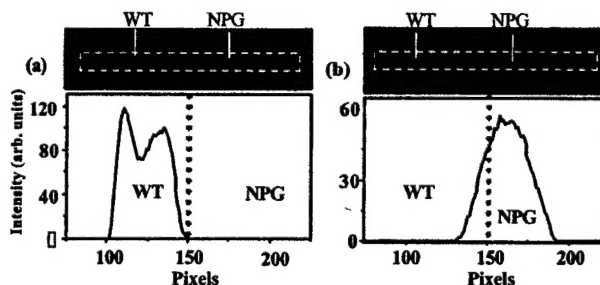


Fig. 2 Time-sliced images of the parotid gland tissue specimen at the gate position of (a) 50 ps, and (b) 250 ps.

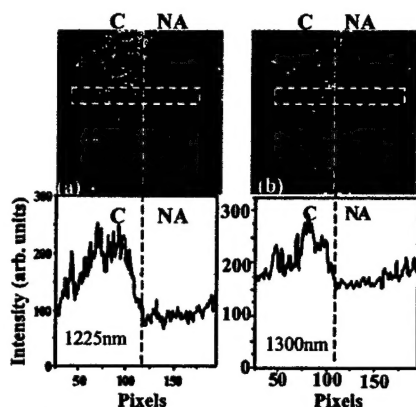


Fig. 3 Spectroscopic images of the breast tissue sample at the wavelength of (a) 1225 nm, and (b) 1300 nm.

cancer (C) region compared to the normal (N) region for both the wavelengths. This indicates higher overall light transmission through the tumor than through normal tissue. A more interesting parameter is the average value of the tumor-to-normal intensity ratio $R_{TN}(\lambda)$ as a function of wavelength. The value of R_{TN} is approximately 2.2 at 1225 nm and 1.5 at 1300 nm, a significant difference.

Similar behavior is observed in the spectroscopic images of the Warthin's tumor (WT) and normal parotid gland (NPG) tissues displayed in Figs. 4(a) and 4(b). The value of R_{TN} is approximately 2.9 at 1225 nm and 1.7 at 1285 nm, again a significant difference.

3.3 Nuclear magnetic resonance imaging



Fig. 6 Histological map of the breast tissue sample showing normal adipose (NA), and cancerous (C) region.

the lower left part has extra-cellular collagen matrix with some interspersed cells, and the much lighter upper right part is rich in normal adipose (NA) tissues. The histology results are consistent with the optical imaging and NMR results. Similar validation of optical imaging results for the parotid gland tissue specimen was also obtained from histological analysis.

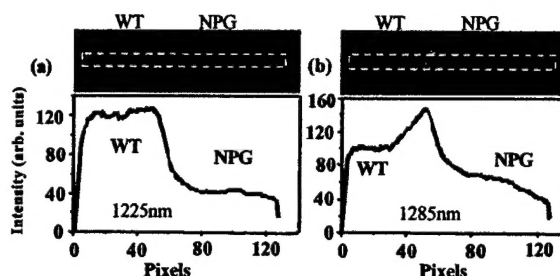


Fig. 4 Spectroscopic images of the parotid gland specimen at the wavelength of (a) 1225 nm, and (b) 1285 nm.

area in all images appear in the respective lower frames. The salient feature of the images is the higher brightness of the



Fig. 5 NMR images of T_1 relaxation time of the 5-mm thick breast tissue sample, (a) first 2.5-mm axial section, and (b) second 2.5-mm axial section.

NMR T_1 -weighted images of the breast tissue specimen are shown in Fig. 5(a) and 5(b). Each figure represents an axial planar image of a 2.5-mm thick region of the sample. Repetition time (TR) for obtaining these images was 500-ms which is greater than 300-ms, the lower limit required for a good contrast/noise ratio (CNR).[13] Echo time (TE) was 16-ms much shorter than 80-ms that also implies a fairly good effective-contrast.[13] The T_2 -weighted images showed no further improvements in image contrast.

For even further validation of the optical imaging results, we obtained histological micrographs of both the breast and the parotid gland samples. Figure 6 shows a histological micrograph of the breast tissue sample. The upper left part that appear much denser than the rest of the micrograph has an abundance of cancer cells (C), the lower left part has extra-cellular collagen matrix with some interspersed cells, and the much lighter upper right part is rich in normal adipose (NA) tissues. The histology results are consistent with the optical imaging and NMR results. Similar validation of optical imaging results for the parotid gland tissue specimen was also obtained from histological analysis.

4. DISCUSSION

The results of both the time-sliced imaging and spectroscopic imaging experiments show the ability of the optical imaging methods to select between the tumor and normal tissues. Images recorded with the earlier arriving light highlighted the tumor, while those recorded with later arriving light accentuated the normal region. The normal upper

right part of the breast specimen was mostly adipose tissue. However, we have observed similar time-dependent difference in light transmission between cancer and normal fibrous breast tissues as well.[5,14] Our observation is that for the same thickness of tissues, light arrives earliest through the cancerous tissue, next through normal fibrous tissues, and latest through the adipose tissues in a breast tissue specimen. Similar, time-dependent transmission was observed for Warthin's tumor and normal parotid gland tissues.

Spectroscopic imaging results are encouraging and may be useful in obtaining diagnostic information. In particular, the wavelength-dependent tumor-to-normal transmitted intensity ratio $R_{TN}(\lambda)$ has the potential to be a useful parameter in tumor identification. Extensive data with different types of cancer will be needed to establish this potential.

Validation of optical imaging results is an important consideration. While pathology is ideal for validation of *ex vivo* measurements, an alternative is needed for *in vivo* applications. Magnetic resonance imaging carried out simultaneously with the optical imaging measurements seems promising for validation of *in vivo* measurements. In summary, time-resolved spectroscopic imaging has the ability to detect tumors in tissues and will be useful in 3-D image reconstruction.

ACKNOWLEDGEMENTS

The work was supported in part by U.S. Army Medical Research and Materiel Command under DAMD 17-98-1-8147, as well as, by NYSTAR.

REFERENCES

1. J. C. Hebden, S. R. Arridge, and D. T. Depty, "Optical imaging in medicine: I. Experimental techniques," *Phys. Med. Biol.* **42**, 841-853, 1997.
2. For a brief review of different optical imaging techniques for biomedical applications see, S. K. Gayen and R. R. Alfano, "Emerging optical biomedical imaging techniques," *Opt. Photon. News* **7**(3), 17-22, 1996.
3. D. Grosenick, H. Wabnitz, H. Rinneberg, K. T. Moesta, P. Schlag, "Development of a time-domain optical mammography and first in vivo applications," *Appl. Opt.* **38**, 2927-2943, 1999.
4. B. Chance, M. Cope, E. Gratton, N. Ramanujam, and B. Tromberg, "Phase measurement of light absorption and scatter in human tissues," *Rev. Sci. Instr.* **69**, 3457-3481, 1998; and relevant references therein.
5. S. K. Gayen, M. Alrubaiee, M. E. Zevallos, and R. R. Alfano, "Temporally and spectrally resolved optical imaging of normal and cancerous human breast tissues," Proceedings of Inter-Institute Workshop on *In Vivo* Optical Imaging at the NIH, Amir H. Gandjebakhche, ed. (Optical Society of America, Washington, DC, 2000), pp. 142-147.
6. S. K. Gayen, M. Alrubaiee, H.E. Savage, S. P. Schantz, and R. R. Alfano, "Parotid gland tissues investigated by picosecond time-gated and optical spectroscopic imaging techniques," *IEEE J. Select. Top. Quantum Electron.* **7**, 906-911, 2001.
7. W. Cai, S. K. Gayen, M. Xu, M. Zevallos, M. Alrubaiee, M. Lax and R. R. Alfano, "Optical tomographic image reconstruction from ultrafast time-sliced transmission measurements," *Appl. Opt.* **38**, 4237-4246, 1999.
8. S. K. Gayen, M. E. Zevallos, M. Alrubaiee, and R. R. Alfano, "Near-infrared laser spectroscopic imaging: a step towards diagnostic optical imaging of human tissues," *Laser Life Sci.* **8**, 187-198, 1999.
9. Q. Fu, F. Seier, S. K. Gayen and R. R. Alfano, "High-average-power kilohertz-repetition-rate sub-100-fs Ti:sapphire amplifier system," *Opt. Lett.* **22**, pp. 712-714, 1997.
10. J. J. Dolne, K. M. Yoo, F. Liu and R. R. Alfano, "IR Fourier space gate and absorption imaging through random media," *Laser Life Sci.* **6**, 131-141, 1994.
11. Jason A. Koutcher, Monica Motwani, Kristen L. Zakian, Xiao-Kui Li, Cornelia Matei, Jonathan P. Dyke, Douglas Ballon, Hyok He Yoo, and Gary K. Schwartz "The *in vivo* effect of bryostatins-1 on paclitaxel-induced tumor growth, mitotic entry, and blood flow," *Clin. Cancer Res.* **6**, 1498-1507, 2000.
12. J. S. Cohen, J. W. Jaroszewski, O. Kaplan, J. Ruiz-Cabello and S. W. Collier "A history of biological applications of NMR spectroscopy," *Progr. NMR Spectrosc.* **28**, 53-85, 1995.
13. J. W. Eveson and R. A. Cawson, "Warthin's tumor (cystadenolymphoma) of salivary glands: a clinicopathologic investigation of 278 cases," *Oral Surg. Oral Med. Oral Pathol.* **61**, 256-262, 1986.
14. S. K. Gayen and R. R. Alfano, "Sensing lesions in tissues with light," *Opt. Express* **4**, 475-480 (1999).